Dynamics of Early Neoproterozoic accretion, west-central India: I. Geochronology and Geochemistry

Anwesa Banerjee, Nathan Cogné, Nicole Sequeira, Abhijit Bhattacharya

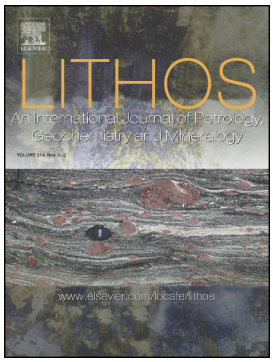

Dynamics of Early Neoproterozoic accretion, west-central India: I. Geochronology and Geochemistry

Anwesa Banerjee, Nathan Cogné, Nicole Sequeira, Abhijit Bhattacharya

PII: S0024-4937(22)00124-4

DOI: https://doi.org/10.1016/j.lithos.2022.106715

Reference: LITHOS 106715

To appear in: *LITHOS*

Received date: 9 December 2021

Revised date: 19 April 2022

Accepted date: 19 April 2022

Please cite this article as: A. Banerjee, N. Cogné, N. Sequeira, et al., Dynamics of Early Neoproterozoic accretion, west-central India: I. Geochronology and Geochemistry, *LITHOS* (2021), https://doi.org/10.1016/j.lithos.2022.106715

Dynamics of Early Neoproterozoic accretion, west-central India: I. Geochronology and Geochemistry

Anwesa Banerjee[1*], Nathan Cogné[2], Nicole Sequeira[3], Abhijit Bhattacharya[1]

[1]Departent of Geology and Geophysics, Indian Institute of Technology, Kharagpur 721 302, India

[2]Univ Rennes, CNRS, Geosciences Rennes, UMR 6118, 35000 Rennes, France

[3]School of Earth, Ocean and Atmospheric Sciences, Goa University, Taleigao Plateau, Goa, 403206, India

[*]Corresponding author

Email ID:anwesabanerjee91@gmail.com

Phone: +91-9932389411

ABSTRACT

The Godhra-Chhota Udepur (GC) sector (west-central India) is the zone of convergence between two crustal-scale accretion zones, i.e. the N/NNE-striking Aravalli Delhi Fold Belt (ADFB) against the E-striking Central Indian Tectonic Zone (CITZ). In this study, we demonstrate the two orogens welded during the Early Neoproterozoic.

In the GC sector, recumbently folded basement gneisses, shallow-dipping granitoid mylonites and a suite of allochthonous supracrustal rocks experienced top-to-the south thrusting and nappe formation (D2 deformation). The shallow-dipping crustal domain was modified by the superposition of a network of WNW/W-striking transpressional shear zones and related folds (D3 deformation). The D2-D3 deformations occurred due to oblique crustal convergence marked by the emplacement of pre-D2, post-D2 and syn-D3 granitoids. The post-D2, syn-D3 granite-granodiorites are weakly peraluminous, calc-alkalic, having ferroan to magnesian affinity, and characterised by LREE-enriched moderately fractionated REE patterns with variable negative Eu anomalies. Trace element geochemistry and whole rock Sr-Nd systematics suggest the granitoids were derived from dominantly meta-greywacke precursors.

In South-GC, U-Pb zircons in the basement gneisses yield upper intercept/Concordia dates at 1.65–1.60 Ga for high-grade metamorphism. The lower intercept/Concordia dates in the gneisses coincide with the 0.95–0.93 Ga emplacement age of post-D2/syn-D3 granitoids throughout GC. However, the pre-D2 granitoids in South-GC are older, ~1.03 Ga. By contrast, pre-D2 granitoids in North-GC yield Late Neoarchean (2.5 Ga) Concordia/upper intercept emplacement ages, identical to the emplacement age of the Archean granites in the ADFB; the lower intercept/Concordia age is 0.95–0.93 Ga. The 2.5 Ga granites did not experience the 1.65–1.60 Ga high-grade metamorphism, but both the lithodemic units shared the 0.95–0.93 Ga D2-D3 deformation-metamorphism and the emplacement of post-D2 and

syn-D3 0.95–0.93 Ga granitoids. The juxtaposition of the ~2.5 Ga granitoids and the 1.65–1.60 Ga gneisses is attributed to the 1.03–0.93 Ga ADFB-CITZ oblique accretion that involved contemporaneous emplacement of syn-collisional S-type granitoids. (300 words)

Keywords: Aravalli-Delhi Fold Belt; Central Indian Tectonic Zone; Archean granites and Paleoproterozoic gneisses; Early Neoproterozoic accretion, syn-collisional granitoids

1. INTRODUCTION

The dynamics of accretion-induced processes of superposed deformation, shear zone nucleation, magma generation and emplacement, and thermal perturbations are best understood at juxtapositions and terminations of orogenic belts (Goscombe et al., 2017). These key locales are a storehouse of natural processes, and analyses of these processes are crucial for understanding the dynamical aspects of accretion of disparately evolved crustal blocks at a global scale vis-à-vis Supercontinent assembly. Granitoid suites from such key locales have been extensively used as proxies to understand crustal evolutionary histories (Hinchey, 2021).

The Great Indian Proterozoic Fold Belt (GIPFOB; Leelanandam et al., 2006) is considered to be a crustal-scale (~1600 km long) tectonic zone. The highly-tectonized zone seemingly "bends" around the North India Block (NIB) which comprises the crescent-shaped Archean Bundelkhand Craton (Fig. 1). The E-striking southern arm of the GIPFOB, also termed as the Central Indian Tectonic Zone (CITZ) (Sharma, 2009) is sandwiched between the NIB and the South India Block (SIB) consisting of the Archean Cratons of Singhbhum and Bastar. This arm consists of the coherently evolved Late Paleoproterozoic to Early Neoproterozoic crustal domains of the Chottanagpur Gneiss Complex (CGC) and the southern and central domains of the Satpura Mobile Belt (SMB), extending west up to the Godhra-Chhota Udepur sector (Banerjee et al., 2021, 2022a). On the other hand, the N/NNE-striking western arm of the GIPFOB comprises the Neoarchean to Early Neoproterozoic Aravalli Delhi Fold Belt (ADFB) juxtaposed between the Marwar Craton (MC) in the west, and the NIB in the east (Fig. 1).

Banerjee et al. (2021, 2022a) demonstrate that the curvilinear geometry of the GIPFOB is not due to the bending of a single accretion zone around an "indentor" (cf. Weil and Sussman, 2004) such as the Bundelkhand Craton. Instead the broad "bend" in the

southern parts of the ADFB is the result of the juxtaposition of two Early Neoproterozoic accretion zones, with the older N/NNE-striking ADFB terminating against the E-striking southern arm or the CITZ with sinistral kinematics (Banerjee et al., 2021, 2022a), similar to the ones reported elsewhere (cf. Macedo and Marshak, 1999; Velandia et al., 2020). But the dynamics of the Early Neoproterozoic accretion of the two orogens are unexplained primarily due to the lack of robust geochronological data of the lithodemic units and geochemical data of the expansive Early Neoproterozoic granitoids that partly obscure the accretion zone. We aim to address this issue in a set of two articles in sequel, of which this manuscript is the first part. In this part, we present the results of the analyses of (i) mesoscale structures, (ii) Laser Ablation Inductively Coupled Plasma Mass Spectrometric (LA-ICP-MS) U-Pb zircon dating, (iii) electron probe microanalysis (EPMA) monazite dating, (iv) whole rock major and trace element geochemistry and (v) Rb-Sr and Sm-Nd isotope compositions in granitoids. The Godhra-Chhota Udepur (GC) sector, where the two accretion zones converge (Banerjee et al., 2021, 2022a), has thus been adopted for this study.

2. GEOLOGICAL BACKGROUND

Four lithodemic units constitute the Precambrian crystalline rocks in the Godhra-Chhota Udepur sector (Fig. 2). The sector is dominated by variably deformed (massive, foliated, mylonitic) blastoporphyritic granitoids, collectively termed as the "Godhra granite" (Gupta et al., 1995). Some of the granitoids are intrusive into poly-deformed anatectic quartzofeldspathic gneisses (Mamtani and Greiling, 2005). The next dominant lithodemic unit comprises greenschist/epidote-amphibolite facies white mica-chlorite schists, micaceous quartzite, foliated and gneissose meta-carbonates, Mn-rich horizons, meta-arenites, deformed oligomict conglomerates and amphibolites of the Champaner Group of the Aravalli Supergroup (Fig. 2a). The Champaner Group of metasediments (Gupta et al., 1995; Joshi and

Limaye, 2014) were previously thought to share an erosional contact with the anatectic gneisses and granitoids but some units of the Godhra granite were however inferred to be intrusive into the supracrustal unit (Joshi and Limaye, 2014). Some ultramafic rocks (pyroxenite, serpentinite) of unknown association also occur in the eastern part of the GC Sector near Jobat (Fig. 2a). The Lunavada Group of the Aravalli Supergroup consisting of greenschist facies quartzite, phyllite, schist and minor carbonates (Gupta et al., 1995) occur to the north of the Godhra-Chhota Udepur Sector (Fig. 2a). The Precambrian crystalline rocks in the southern part of the GC sector are obscured by the Upper Cretaceous Deccan volcanics, the infratrappean Lameta Formation and the intertrappean Bagh beds (terminology after Sahni et al., 1994) (Fig. 2a).

The emplacement ages of the Godhra granite vary between Late Mesoproterozoic to Early Neoproterozoic, e.g. 955 ± 20 Ma, (Rb-Sr, Gopalan et al., 1979), 1168 ± 30 Ma (Rb-Sr, Srimal and Das, 1998), 965 ± 40 Ma, (Rb–Sr, Goyal et al., 2001), and 1050 ± 50 Ma, (Sm–Nd, ShivKumar et al., 1993). The 955 Ma age of Gopalan et al. (1979) is the most cited age for the emplacement of the Godhra granite (Mamtani and Greiling, 2005 and references therein). Recently Banerjee et al. (2022a) carried out U-Pb LA-ICP-MS zircon dating of an anatectic gneiss and a blastoporphyritic granite. The high-grade anatexis-metamorphism in the anatectic gneiss occurred at ~1.65 Ga, and the emplacement age of the granitoid was 0.95–0.90 Ga, consistent with the existing Early Neoproterozoic Rb-Sr and Sm-Nd isochron dates in the Godhra granite.

The lithological, field relation and analysis of mesoscale to regional structures and deformation kinematics are discussed by Banerjee et al (2021, 2022a, and 2022b, accompanying article). In this section, we highlight the structural aspects vis-à-vis stages of granitoid emplacement relevant to this article (Fig. 3a). The most significant feature in the GC sector is a shallowly-dipping to gently-inclined structural domain (D2 deformation)

composed of mylonitic to foliated granitoids, recumbently folded anatectic gneisses and the Champaner group of greenschist to amphibolite facies supracrustal rocks (Fig 3b, c) inferred to be an allochthonous unit (Banerjee et al., 2022a). The W/WNW-plunging D2 recumbent folds in the gneisses formed on D1a, b metatexite layers; limited syn-D2 anatexis (<2 vol% of rock) was observed in a couple of biotite-rich gneiss outcrops. By contrast, the W/WNW-plunging D2 folds in the supracrustal rocks formed on a pre-D2 axial planar fabric defined by the shape preferred aggregates of white mica-chlorite assemblages in mica schists, talc-tremolite-antigorite in meta-carbonate, and amphibole-plagioclase-clinozoisite-chlorite in amphibolites (details in accompanying article; Banerjee et al., 2022b). The hinges of D2 folds in the gneisses and rocks in the supracrustal unit are broadly collinear with the D2 stretching lineation in the pre-D2 granitoids (Fig. 3b, c).

The shallow-dipping tectonic mélange formed by top-to-the-south thrusting of the supracrustal rocks over the basement rocks leading to the folding and interleaving of the rock units (Fig. 3a). The tectonic mélange is traversed by a network of W/WNW-striking steep-dipping transpressional shear zones (D3) with sinistral and dominantly N-down kinematics (Fig. 3a); S-down movement along the D3 shears occur in a few outcrops. In the vicinity of these D3 shears (Fig. 3d, e) the gneisses and the supracrustal rocks exhibit upright folds and the granitoids evolve into steep-dipping L and L-S tectonites (Fig. 2b). Locally-developed steep-dipping conjugate shear zones (D4) striking NNE (dextral) and ENE (sinistral) in the D4 high-strain zones are melt-hosted within the granite mylonites, and are deemed to be coeval with the D3 deformation (Fig. 2a). As with the D2 deformation event, the D3 stretching lineations and broadly collinear D3 fold axes plunge at low to moderate angles to the W and WNW (Banerjee et al., 2022a). The thrust-dominated (D2) and wrench-dominated (D3) deformations are inferred to be a part of the progressive NNE-SSW crustal shortening that caused orogen-parallel stretching (Banerjee et al., 2022a).

The granitoids in the area are dominantly post-D2 to syn-D3; the granitoids occur as lens-shaped bodies, exemplified by the Sanada granitoid pluton (Fig. 2a; Banerjee et al., 2022a). The pre-D2 granitoids cover a smaller area. Post-D3 granites are lacking in the Godhra-Chhota Udepur sector. All structural types of granitoids are blastoporphyritic, foliated and dynamically recrystallized. The pre-D2 granitoids possess a prominent tectonic foliation (D2) and contain cm-sized elliptical to round K-feldspar porphyries that constitute <2 vol% of the rock (Fig. 4a). Some of the pre-D2 granitoids are found to be interleaved with the anatectic gneisses, and the D2 foliation in the granitoid is axial planar to the D2 folds in the gneisses (Fig. 4b). In the post-D2 granitoids, K-feldspar porphyries are euhedral to subhedral, large (long axes up to 6 cm) and constitute up to 50 vol% of rock in the interiors of E-W striking plutons (Fig. 4c). In these granitoids, trains of euhedral K-feldspar porphyries and imbrications among euhedral porphyries are inferred to be magmatic flow textures; tectonic fabrics in these granitoids are weakly developed or lacking. But towards the pluton margins, the flow-textured and massive granitoids grade into intensely foliated (steep-dipping D3) varieties (Fig. 4d). In the syn-D3 granitoids, K-feldspar porphyries constitute up to 75% of the rock, and trains and imbrications among large euhedral K-feldspar porphyries dominate the rocks. Some of these porphyries develop asymmetric tails (sinistral sense) that are drawn out sub-parallel to quartz lentils and aggregates of shape-preferred biotite flakes forming the warping D3 foliation (Fig. 4e). The pre-D2 granitoids are sometimes preserved as small relicts within the post-D2 and the syn-D3 granitoids that exhibit intrusive margins; at other places mineralogically different types of granitoids share sharp contacts (Fig. 4f).

2.1 **Deformation microstructures in granitoids**

The granitoids within the D2 shallow-dipping domains are fine to medium grained, well-foliated and contain porphyries of subhedral feldspar (Fig. 5a). The D2 foliation in the rocks

is primarily defined by the shape-preferred biotite flakes (Fig. 5a; hornblende is rare), and xenoblastic mono- and poly-crystalline quartz lentils, commonly exhibiting strain wavy extinction and sub-grains (Fig. 5b); the mosaic of dynamically recrystallized alkali feldspar (microcline), plagioclase and internally-strained quartz grains share serrated (high energy) grain and phase boundaries (Fig. 5b, c), and are anchored to the D2 biotite and quartz lentils (Fig. 5c). Triple junctions among feldspar are rare. Coarse porphyries of magmatic K-feldspar and plagioclase within the finer grained mineral mosaic exhibit patchy chemical zoning and core-mantle structures; the margins of these feldspar grains exhibit serrated to lobate-cuspate margins against the quartz grains (Fig. 5d). By contrast, the post-D2 granitoids are invariably coarse-grained, weakly foliated, and blastoporphyritic (Fig. 5e). The D3 fabric in the granitoids is defined by trains and imbrications among euhedral feldspar grains (Fig. 5f), crude alignment among flaky biotite, and internally strained quartz lentils; the quartz lentils have smaller aspect ratio (length/width) relative to those in the pre-D2 granitoids. The foliation is somewhat sinuous and wraps around coarser microcline phenocrysts within the mosaic of recrystallized minerals. The feldspar grains are weakly-strained internally and largely preserve their magmatic shapes (Fig. 5f). But within the mosaic, these feldspar grains share lobate-cuspate margins against the quartz lentils which in turn commonly show chess-board sub-grain structures (Fig. 5g). Intensely sheared post-D2 granitoids exhibit mylonitic fabric defined by internally strained quartz ribbons, and core-mantle structured dynamically recrystallized feldspars that share lobate-cuspate grain and phase boundaries against other minerals (Fig. 5h).

Overall, the post-D2 granitoids are weakly strained relative to the pre-D2 granitoids in the shallow-dipping carapace; this is manifested by the finer grain size and the paucity of relic magmatic porphyries in the pre-D2 granitoids. But the common occurrences of chess-board microstructures in quartz suggest the post-D2 granitoids were hot (T> 650 ºC; Kruhl, 1996)

during D3 deformation. Chess-board microstructures in quartz in the post-D2 granitoids are highlighted by several authors (Mamtani and Greiling, 2005; Banerjee et al., 2022a); by contrast the pre-D2 granitoids lack this deformation microstructure. If we therefore combine the mesoscale field relations with the deformation microstructures, the emplacement of the post-D2 granitoids appears to be broadly synchronous with the D3 deformation induced by the N-S convergence, but this deformation outlasted the solidification of the post-D2 granitoids.

3. GEOCHRONOLOGY

In this section, we present Laser Ablation ICP-MS U-Pb zircon dates in nine structurally constrained samples (2 anatectic gneisses, and 7 granitoids) and chemical dates from monazite in four samples (2 anatectic gneisses and 2 granitoids) obtained from different parts of the Godhra-Chhota Udepur sector (locations in Fig. 2b). A brief summary of mineral assemblages, texture, zircon and monazite morphology in the 13 samples used in geochronology are presented in Table 1. The results are designed to constrain the age of the different magmatic, metamorphic and deformation events crucial for a tectonic restoration of the dynamics of accretion between the ADFB and the CITZ orogenic belts. In the nine samples, cathodoluminescence (CL) images of representative zircons along with the analyzed spots and corresponding $^{207}Pb/^{206}Pb$ dates are shown in Fig. 6. Throughout the text, figures and tables, the uncertainties are shown at 2σ level. The concordia plots are shown in Fig. 7. Representative monazite X-ray elemental images with embedded spot dates in Ma, BSE images depicting textural setting of the monazite grains and probability-density plots showing mean populations dates (in Ma) are shown in Fig. 8. Fig. 2b provides the spatial distribution of the zircon dates obtained in this study and those in the two samples analyzed by Banerjee et al. (2022a).

3.1 Zircon geochronology

LA-ICP-MS U-Pb zircon dating was performed on two gneisses (AW 161, AW 114) and seven pre-D2 to syn-D3 granitoids (AW 98, AW 145, AW 127, AW 18, AW 73, AW 8, AW 9A). The zircon grains were analyzed at the Plateforme GeOHeLiS, Géosciences Rennes, University of Rennes, France. The analytical procedure and instrument operating conditions are detailed in the Appendix A. Zircons from both the gneiss and granite samples are large (~200–300 μm long), well-faceted, prismatic to square in shape, and pink to honey-yellow in colour (details of individual samples are in Table 1a). Plots of Th/U vs. $^{207}Pb/^{206}Pb$ ages in zircons are shown in Fig. 6a. CL images of the zircons show oscillatory zoning (alternating light and dark bands surrounding a core), patchy zoning (localized clusters of bright domains in a homogenous dark grain), overgrowths truncating earlier zoning or completely recrystallized textures (dark CL response, no texture) (Fig. 6b–i). Age spots were analyzed in each of these domains. The U-Pb analysis and the age data obtained from the individual samples are provided in Supplementary Material[1] and a brief description of each sample is provided in Table 1a and discussed below. All uncertainties are quoted at 2σ level; see Appendix for details about propagation of uncertainties.

3.1.1 Gneisses:

Sample AW 161 is a quartzofeldspathic gneiss. The prominent mineral segregation banding in the rock bears one set of prominent D3 tight to open folds with steep dipping E-W striking axial planes and moderate plunge to the WNW. Pre-D3 folds are rare, but metatexite layers are lacking. A total of 35 spots were analyzed in 23 zircon grains. The zircon grains do not show prominent core-rim structures in the CL images (Fig. 6b). Th/U ratios of the grains vary in the range 0.04–1.60 (Fig. 6a); the values <0.1 (4 points) correspond to CL-dark zones.

Two spots from the same grain (CL-dark zone, Th/U ~ 0.04) furnish concordant age of 909 ± 11 *(±36)* Ma (MSWD = 0.51; Fig. 7a). On the other hand, 33 of the 35 analyzed spots describe a well-defined Discordia with the upper intercept at 2485 ± 15 *(± 96)* Ma and the lower intercept at 932 ± 15 *(± 39)* Ma (MSWD = 1) (Fig. 7a). The younger date (~0.93 Ga) is inferred to be the age of deformation-metamorphism in the rock; the older date (~2.5 Ga) corresponds to either the age of formation of the rock or the age of inherited zircons in the rock.

Sample AW 114 is an anatectic gneiss from a D3 high-strain domain in the southern part of the GC sector (Fig. 2b). The metatexite gneiss comprising alternate biotite-rich and leucosome layers describe prominent D2 recumbent folds. The metatexite layers are pre-D2. The recumbent folds are wrapped by locally penetrative isoclinal to tight folds forming a ramp and flat structure related to the D4 dextral shears. A total of 25 spots were analyzed in 24 grains in the sample. Most of the grains show core-rim textures, although some grains are homogenous, recrystallized and appear dark in CL images (Fig. 6c). The Th/U ratios of the zircon grains vary from 0.04–1.25 (Fig. 6a), the values <0.2 correspond to CL dark domains and are mostly from the recrystallized and homogenous grains. All the 25 spots define a Discordia with upper intercept date of 1742 ± 20 *(± 69)* Ma and a lower intercept date of 470 ± 30 *(± 35)* Ma (MSWD = 0.41; Fig. 7b). We consider that the Pan African lower intercept date (~0.5 Ga) has no physical significance in view of the fact that monazites which are especially susceptible to fluid-induced alteration even at greenschist facies condition does not yield dates younger than Early Neoproterozoic in the diverse lithodemic units (including anatectic gneisses) from the GC sector examined by Banerjee et al. (2021) and in this study (see later).

3.1.2 Granitoids:

Two samples, AW 18 and AW 145, are post-D2 blastoporphyritic granitoids sampled from D3 high strain domains (Fig. 2b). Sample AW 18 is the northernmost dated sample of pink blastoporphyritic granitoid neighboring Godhra; the alignment of euhedral K-feldspar porphyries defines N110° striking magmatic fabric. Sample AW 145 is a weakly foliated pink granitoid consisting of K-feldspar porphyries and biotite defining the N110° steep fabric. Sample AW 98 is a granite phyllonite with steep NNE-trending fabrics corresponding to the D4 shears.

Thirty spots were analyzed in 15 grains from the sample AW 18. The zircon grains show well developed core-rim structures with oscillatory zoning (Fig. 6d). Th/U ratios in these grains vary from 0.3–1.91 (Fig. 6a), except for 2 spots with Th/U ratio of 0.16 and 0.18 corresponding to two CL-dark rims of zircon grains. Seven concordant analyses yield a concordia age of 946 ± 6 *(± 37)* Ma (MSWD = 0.54; Fig. 7c). These seven points lie at the upper intercept of a Discordia defined by seventeen other spots from both cores and rims of zircon grains (Fig. 7c). The lower intercept of the Discordia does not have significance. No difference in dates could be deciphered between the core and rims of the zircon grains.

In the sample AW 145, 35 spots were analyzed in 19 grains (Fig. 6d). The Th/U ratios of the analyzed spots range from 0.37–2.52 (Fig. 6a), with only three spots marked by Th/U ratios <0.1. These three spots pertain to CL-dark domains within the zircon grains and yield highly discordant ages and have not been considered. Twelve concordant spots yield a concordia age of 955 ± 7 *(± 37)* Ma (MSWD = 1.2) and define a Discordia with 8 other points with an upper intercept at 2525 ± 46 *(± 106)* Ma and lower intercept at 944 ± 15 *(± 39)* Ma (MSWD = 1; Fig. 7d). The overlapping concordia and lower intercept dates correspond to the post-D2 emplacement age of the granitoid, whereas the Neoarchean upper intercept date possibly represents the age of the protolith.

A total of 30 spots in 14 grains were analyzed in sample AW 98. The analyzed spots mostly have high common lead and their Th/U ratios range from 0.09–1.82. No alignment is found in the Wetherill plot (Fig. 7e). However, two concordant spots (shown in pink colour in Fig. 7e), with no common lead, and Th/U ratio of 0.39 and 0.43 (Fig. 6a) are obtained with $^{207}Pb/^{206}Pb$ dates of 2418 ± 30 Ma and 2384 ± 30 Ma respectively (Fig. 6f) that possibly correspond with the age of emplacement (~2.4 Ga) of the granitoid.

Sample AW127 is pink granitoid collected from a large outcrop in the Orsang river bed south of Bodeli in the southern GC sector (Fig. 2b). The granitoid is very coarse-grained and studded with end-to-end touching and imbricate grains of large (> 6cm long crystals), euhedral to subhedral, un-recrystallized K-feldspar laths exhibiting zoning and Carlsbad twins. An ill-defined steep E-striking D3 fabric in the rock is described by trains of feldspar laths. The weak planar fabric, the coarse-grained nature of the granites, and the unrecrystallized feldspar laths suggest that the rock represents the last episode of granite emplacement in the region. Twenty-five spots have been analyzed in 21 zircon grains (Fig. 6g). Seven of the 25 spots furnished a concordant date of 951±10 *(± 37)* Ma (MSWD = 1.2; Fig. 7f). All the seven spots are from the rims of the zircon grains while the cores yield discordant dates. This date is inferred to correspond to the emplacement age of the syn-D3 granitoid.

Sample AW 9A is a massive (no mesoscale fabric) post-D2 white coloured granitoid impoverished in ferromagnesian minerals. The sugary appearance of the rocks is due to dynamic recrystallization of feldspars. The granite is apophytic into an ensemble of multiply-deformed quartzofeldspathic and interleaved calc-silicate gneisses that experienced multiple deformation events. A total of 30 spots were analyzed in 13 grains (Fig. 6h). Although most of the analyzed spots are discordant and have some amount of common lead, 2 spots from the

CL-dark core of a zircon grain yield a concordant date of 1607 ± 24 Ma (MSWD = 0.40) while a single concordant analysis with $^{206}Pb/^{238}U$ date of 951 ± 17 Ma is obtained from the CL-dark core of another zircon grain. A Discordia is defined with four spot ages (no common lead, Th/U ratios between 0.26–0.79, all from cores of zircon grains, with an upper intercept age of 2544 ± 82 *(± 127)* Ma and a lower intercept age of 958 ± 26 *(± 45)* Ma (MSWD = 0.88; Fig. 7g). The youngest dates (951 ± 17 Ma, 958 ± 26 Ma) in the deformed and recrystallized granite with no mesoscale fabric possibly correspond with the age of emplacement of the intrusive. The older date at ~1.61 Ga closely corresponds to the age of high-grade metamorphism in the anatectic gneisses (Banerjee et al., 2021); the ~2.54 Ga date is coeval with the emplacement age of the granite or the protolith age of the gneisses in the northern part of the GC sector. Notably though no Discordia exists between 2.54 Ga and 1.61 Ga.

Two pre-D2 grey-coloured granitoids were dated from the southern domain, AW 8 and AW 73 (Fig. 7h). The sample AW 73 is from a large hillock, whereas AW 8 was sampled from a hummocky sheeted outcrop. Both samples are characterized by low proportions (< 2 vol%) of cm-sized circular-shaped K-feldspar phenocrysts and high modal amounts of biotite. The rocks possess biotite-defined weak shallowly-dipping D2 fabrics in a mosaic of dynamically recrystallized feldspars and quartz.

For AW 73 (Fig. 6i), 40 spots were analyzed in 18 grains and no concordant spots were obtained. However, 29 spots define a Discordia with upper and lower intercepts at 1026 ± 17 *(± 43)* Ma and 111 ± 40 *(± 40)* Ma (MSWD = 1.4; Fig. 7h). In sample AW 8 (Fig. 6j), 40 spots were analyzed in 22 grains. Three spots from the rims of three zircon grains yield a concordant date of 983 ± 11 *(± 39)* Ma (MSWD = 1.4; Fig. 7i). These three spots along with 21 other spots corresponding to both cores and rims of zircon grains define a Discordia with upper and lower intercepts at 1020 ± 22 *(± 45)* Ma and 186 ± 35 *(± 36)* Ma (MSWD = 0.95)

respectively (Fig. 7i). For both the foliated granitoids, the upper intercept (1.03–1.02 Ga) dates are inferred to correspond with the emplacement ages of the granitoids. The significance of the slightly younger concordant dates (~0.98 Ga) obtained from the rims of the zircon grains may correspond with thrusting and associated shallow-dipping fabric formation. The lower intercept dates are not considered to be significant.

3.2 Monazite chemical dating:

Two samples each of anatectic gneisses (AW 7, AW 9B) and grey granitoids (AW 12, AW 163) with steep E-striking D3 fabrics were analyzed for monazite chemical dating following the procedure of Montel et al. (1996) at the Department of Earth Sciences, Indian Institute of Technology Bombay (Powai). A brief description of the methodology is provided in Appendix B. The locations of the analyzed samples are shown in Fig. 2b and the data is presented in Supplementary Material[2]. A brief description of the rocks, textural chemical characteristics, and summary dates in monazite are provided in Table 1b. The monazite grains mostly occur within biotite rich aggregates, and only few monazites are hosted within quartz-feldspar aggregates (Fig. 8a, c, e, g). The grains are ellipsoidal to prismatic, xenoblastic to sub-idioblastic and chemically zoned in Th, Y and U (rarely Pb) (Fig. 8a, c, e. g). Based on X-ray element maps for Th, U, Pb and Y and back-scattered electron images, 58 spot dates were obtained in chemically distinct domains in the four samples. The monazite spot ages in the four samples (Fig. 8b, d, f, h) taken together yield dates between 863 ± 50 Ma to 969 ± 47 Ma, with an average age of around ~ 918 Ma; one outlier spot is dated at 1020 ± 32 Ma. The mean dates obtained for the samples are identical at 2σ level. Anatectic gneisses AW 9B and AW 7 yield mean dates of 923 ± 13 Ma (MSWD = 1.8, n = 11) and 905 ± 16 Ma (MSWD = 3.7, n = 14) respectively (Fig. 8b, d). The granitoid AW 163 yields a

mean date of 908 ± 19 Ma (MSWD = 2.7, n= 12), and 21 spots in the granitoid AW 12 yield a mean date of 926 ± 11 Ma (MSWD = 3.3) (Fig. 8f, h).

3.3 Summary of age data:

The LA-ICP-MS U-Pb zircon dates obtained in the nine samples, combined with two zircon-dated samples in Banerjee et al (2022a), may be grouped into four age populations, e.g. 2.5–2.4 Ga, 1.7–1.6 Ga, 1.03–1.02 Ga and 0.95–0.93 Ga (Fig. 9). The monazite chemical dates in this study and those in Banerjee et al. (2022a) in gneisses, granitoids, and greenschist/amphibolite facies supracrustal rocks overlap with the youngest population of U-Pb zircon dates. The youngest age population (0.95–0.93 Ga) corresponds to the emplacement of the post-D2 granitoids including the syn-D3 granitoids. The age population (1.03–1.02 Ga) corresponds to the emplacement of the younger set of pre-D2 granitoids. Pre-D2 high-grade metamorphism-anatexis in the anatectic gneisses occurred at 1.65–1.6 Ga (cf. Banerjee et al., 2021, 2022a, 2022b). The oldest Concordant and upper intercept Discordia dates (2.5–2.4 Ga) in zircons are obtained from pre-D2 foliated granites and non-anatectic gneisses located in the northern part of the GC sector based on the results of LA-ICP-MS zircon U-Pb analysis from a total of 11 samples (Fig. 2b). There is no evidence to suggest that these Neoarchean/Early Paleoproterozoic rocks, lacking in the southern part of the GC sector, experienced the 1.65–1.60 Ga high-grade metamorphism recorded in the anatectic gneisses (Fig. 2b). The consequences of these observations are discussed in section 5.

4. GEOCHEMISTRY OF 1.03–0.93 Ga GRANITES

4.1 Whole rock major and trace element geochemistry

Whole rock geochemical analyses were performed on 9 pink granitoids, 10 grey granitoids and 5 anatectic gneisses (locations in Fig. 2b). The details of sample processing and protocols

for analyses done by Inductively Coupled Plasma Emission Spectrometry (ICP-ES) for major elements, and Inductively Coupled Plasma Mass Spectrometer (ICP-MS) for trace elements at the ACME Lab, Bureau Veritas, Vancouver, Canada are described in the Appendix C. The results are provided in Table 2 and used in various discrimination plots in Fig. 10. Chondrite normalized REE diagrams and bulk continental crust normalized trace element spider diagrams for the granitoid and gneiss samples are presented in Figs. 11 and 12 respectively.

The major element oxide contents in the pre-D2 ~1.03 Ga granitoids and post-D2 0.95–0.93 Ga granitoids are variable, e.g. SiO_2 (63.27–75.74 wt%), Al_2O_3 (10.15–15.48 wt%), Fe_2O_3 total (0.54–6.17 wt%), MgO (0.32–1.82 wt%), K_2O (2.59–6.88 wt%), Na_2O (0.68–4.8 wt%), CaO (0.24–3.31 wt%), and TiO2 (0.06–1.22 wt%) (Table 2). The Fe# (molar FeO/FeO+MgO) of these granitoids lie between 0.40 and 0.77 (Table 2). The granitoids are granite-granodiorite in composition (Fig. 10a), with the exception of AW 155 which plots in the field for monzonite. The alumina saturation index (ASI) in the granitoids, calculated as molar $Al_2O_3/(CaO+Na_2O+K_2O)$, lies in the range 0.98–1.24; the granitoids therefore are weakly peraluminous (Fig. 10b), with AW 155 (ASI value: 0.86) being the only exception. The granitoids plot in the field of S-type granitoid (Fig. 10c). Within the granitoids, Fe_2O_3 (total), MgO and CaO decrease with increasing SiO_2; Al_2O_3 exhibits a weak negative correlation with SiO_2, and K_2O exhibits the opposite trend (Supplementary Material[3]). The compositions of the anatectic gneisses overlap with those in granitoids; however MgO contents in the gneisses are higher and Fe# are lower relative to the granitoids in the GC sector (Supplementary Material[3]).

The ∑REE in the pink granitoids vary between 108 ppm and 751 ppm; the corresponding value for the grey granitoids range between 84 and 424 ppm (Fig. 10d, Table 2). Sample AW 155 has the highest REE abundance, 1008 ppm (Fig. 10d, Table 2). The chondrite normalized REEs in the granitoids are LREE enriched [$(La/Yb)_{CN}$ = 11–89] and the

HREEs exhibit relatively flat patterns [$(Gd/Yb)_{CN}$ = 1.54–4.67] (Fig. 11). The granitoids are characterised by small but variable negative Eu anomalies (computed as $(Eu_{CN}/Eu^*$; Fig. 11), where Eu* is calculated as $(\sqrt{Sm_{CN}}*Gd_{CN})$ for the pink granitoids and range between 0.08 and 0.83; a grey granitoid (AW 63) has a Eu anomaly value of 1.00 (Table 2; Fig. 10d).

The Nb/Ta values for the GC granitoids (5.2–21.6) are typical for peraluminous granites unmodified by hydrothermal activity (> 5; Ballouard et al., 2016). The negative trend of Nb/Ta versus Ta (Fig. 10e) is attributed to mica fractionation (Ballouard et al., 2016). In the Nb/Ta versus Zr/Hf diagram (Fig. 10f), the GC granitoids plot in the field for peraluminous "barren" granites (Ballouard et al., 2016). On the Th/Ta versus Yb plot (Gorton and Schandl, 2000) (Fig. 10g), some of the pink granites lie in the field of active continental margins; the rest of the granitoids plot in the field of oceanic arcs.

Chondrite normalized REE diagrams and bulk continental crust normalized trace element spider diagrams for the granitoids and gneisses in the GC sector are presented in Figs. 11 and 12 respectively. The trace element abundances of the S-type granitoids normalized to the bulk continental crust composition (Rudnick et al., 2003) show an overall enrichment of incompatible elements in the granitoids (Fig. 12a–b). Similar trace element enrichment is also observed in the gneisses with respect to the bulk continental crust (Fig. 12c). An average gneiss composition (blue bold line in Fig. 12c) for the GC samples also mimics the enriched trend of the gneisses relative to the bulk crust. Assuming the anatectic gneisses were the source rocks for the granitoids (see Discussion), we normalized the granitoid trace element abundances to the average composition of the 5 basement gneisses (Fig. 12d–e). Relative to the average gneiss (Fig. 12c), the pink granitoids are enriched in Ba, Th and LREEs and depleted in P, Eu, Ti and HREEs (Fig. 10d); the grey granitoids on the other hand show enrichment of Rb, Ba, Th, U, K, Nb, Ta and LREEs, and depletion of P, Ti Zr, Hf, Sm, Eu, Y and HREEs (Fig. 12e).

The Zr concentrations of the granitoids were used to calculate the zircon saturation temperature (T_{Zr}) (Clemens, 2003) which may be used as a proxy for obtaining crystallization temperature of the melts (Watson and Harrison, 1983). The T_{Zr} was calculated for the GC granitoids (Table 2) using the formulation of Watson and Harrison (1983) and Boehnke et al. (2013). The average temperature estimate obtained for the pink granitoids is 840 °C and 800 °C by the Watson and Harrison (1983) and Boehnke et al. (2013) formulations respectively; while the T_{Zr} for the grey granitoids vary between 800°C and 760 °C.

4.2 Whole rock Sr-Nd systematic in granitoids

Whole rock Rb-Sr and Sm-Nd isotopic analyses were performed on 4 pink and 3 grey granitoids (Table 3). The methodology is described in Appendix D. The granitoids have a wide range of $^{87}Sr/^{86}Sr$ ratios (0.7156–0.7950). The $^{143}Nd/^{144}Nd$ ratios for these granitoids are tightly constrained between 0.511033 and 0.511407 (Table 3). The εNd(0) for these granitoids are strongly negative (-23.9 to -31.2) (Fig. 13a; Table 3). The εNd(t) at t=1030Ma for pre-D2 granitoids and at t=950 Ma for post-D2 granitoids range from -11.1 to -18.6 (Fig. 13b, Table 3). In the εNd(t) versus T_{2DM} plots (Fig. 13c), the GC granitoids also have negative εNd(t) values. The ranges of T_{CHUR}, T_{DM} and T_{2DM} estimates for the GC granitoids are 1.65–2.18 Ga, 2.05–2.53 Ga and 2.43–3.05 Ga respectively. The T_{DM} and T_{2DM} are better approximations relative to CHUR for most post-Archean rocks since significant amounts of crust formed in the Archean by repeated melt extractions from the mantle (Patchett, 1989). The εNd(t) versus the $^{87}Sr/^{86}Sr$ initial ratios for the GC granitoids (Fig. 13b) also show crustal values ($^{87}Sr/^{86}Sr > 0.706$, εNd negative; Winter, 2001).

5. DISCUSSION

In Table 4, the important mesoscale structural features and the gamut of age data generated in this study and in Banerjee et al. (2022a) are integrated to highlight the significant tectonic features in the Godhra-Chhota Udepur Sector.

5.1 Tectonic interleaving at 1.03–0.95 Ga

The spatial distribution (Fig. 2b) of LA-ICP-MS U-Pb zircon dates obtained in this study (Fig. 7a–i) and by Banerjee et al. (2022a) in the Godhra-Chhota Udepur sector (Fig. 9) reveal intriguing features unknown earlier. First, the Late Neoarchean Discordant upper intercept ages and the Concordant ages in the pre-D2 granitoids are restricted to the northern parts of the sector (Fig. 2b). By contrast, the Late Paleoproterozoic (1.7–1.6 Ga) age of pre-D2 high-grade metamorphism in the anatectic gneisses and the younger Late Mesoproterozoic (~1.03 Ga) pre-D2 granitoids occur exclusively in the southern part. And second, the Discordia lower intercept and the Concordant ages for the emplacement of the post-D2 granitoids (including syn-D3 granitoids) across the north-south divide are tightly constrained between 0.95 and 0.93 Ga. These ages are identical to the ones obtained from the existing Rb-Sr and Sm-Nd isochron ages (Gopalan et al., 1979, Srimal and Das, 1998, ShivKumar et al., 1993, Goyal et al., 2001). In view of the large variations in the emplacements ages of the granitoids, the term "Godhra granite" coined by Gopalan et al., (1979) and adopted by later workers (Srimal and Das, 1998, ShivKumar et al., 1993, Goyal et al., 2001) for the gamut of felsic intrusives in the sector is a misnomer, and needs to be discontinued. It may be recalled that several researchers (Mamtani and Greiling, 2005) based on field investigations had also suggested that the "Godhra granite" is a composite unit (Banerjee et al., 2021, 2022a; this study).

The pre-D2 Neoarchean granitoids with single shallow-dipping tectonic foliation do not exhibit the multiple folds and imprints of the younger Late Paleoproterozoic high-grade metamorphism and anatexis typical of the basement gneisses in the different crustal domains

of the CITZ that extends eastwards from the Godhra-Chhota Udepur sector into the central and southern domains of the Satpura Mobile Belt (SMB) in central India, and the Chottanagpur Gneiss Complex (CGC) further to the east (Banerjee et al., 2021). Also the Late Paleoproterozoic basement gneisses in the Godhra-Chhota Udepur sector do not provide evidence of Neoarchean or older inheritance in the analyzed zircon grains. Yet zircon U-Pb systematics show that both the Neoarchean granitoids and the Late Paleoproterozoic gneisses bear Early Neoproterozoic imprints either as lower intercept Discordia and/or concordant dates, identical to the emplacement ages (0.95–0.93 Ga) of the post-D2 and syn-D3 granitoids (Figs. 7–9).

The Late Neoarchean granitoids are unlikely to be the basement for the younger Late Paleoproterozoic gneisses, for it would be impossible for the Neoarchean granitoids to escape the pervasive 1.65–1.60 Ga metamorphism-anatexis at T ≥750 °C (accompanying article: Banerjee et al., 2022b). It therefore is reasonable to assume that the 2.5–2.4 Ga granitoids are slivers of crustal domains that are tectonically interleaved with the Late Paleoproterozoic gneisses and the younger (~1.03 Ga) granitoids of the CITZ. These chronologically diverse lithodemic units experienced a shared syn to post-D2 history, and were intruded by 0.95–0.93 Ga post-D2 granitoids. We infer, therefore, that the tectonic interleaving of the lithodemic units occurred between ~0.93 Ga (age of post-D2 granitoids) and the 1.03–1.02 Ga pre-D2 granitoids in the tectonic melange.

5.2 1.03–0.93 Ga granitoids: Petrogenesis

Large volumes of S-type magmas maybe generated from melting of metasedimentary protoliths of metagreywacke, metapelitic or metatonalitic compositions (Clemens, 2003). Zhu (2020) argue that turbidite sequences in accretionary prisms comprising banded shale and greywackes undergo melting towards the end of orogenic cycles following initial continent-

continent collision and accretionary prism development to generate S-type magmas. The GC granitoids show high molar $CaO/MgO+FeO_T$ (0.42–0.74) and CaO/Na_2O (0.3–2.5) ratios (Fig. 14a, b) indicating they were mostly derived from plagioclase-rich greywackes; however, a few samples also show relatively low molar $CaO/MgO+FeO_T$ (0.15–0.32) and CaO/Na_2O (<0.1) ratios which are interpreted to be derived from metapelitic melts (Sylvester, 1998). Two granitoids (AW 9A, AW 21) have a high molar $CaO/MgO+FeO_T$ ratio (1.62, 1.54). The post-D2 white-coloured granitoid AW 9A has the highest molar $CaO/MgO+FeO_T$ ratio (1.62) and high molar $Al_2O_3/MgO+FeO_T$ (12.5). The corresponding values for the other granitoid AW-21 are 1.54 and 4.18 respectively. These samples may be derived from source rocks having meta-tonalite affinity (Sylvester, 1998). The GC granitoids thus appear to be melting products of heterogeneous metasedimentary protoliths, dominated by metagreywackes.

The spread in the $^{87}Sr/^{86}Sr$ (0.71564–0.79143) and $^{143}Nd/^{144}Nd$ (0.511033 to 0.511407) ratios (Fig. 13) may also be attributed to this heterogeneity of the protolith characters (Clemens et al., 2009) or may have been caused by mixing with other crustal melts (Collins, 1996). Strongly negative εNd (-22.9 to -31.2) values suggest the derivation of the granitoids from recycled crustal sources. The $^{87}Sr/^{86}Sr_i$ ratios (0.7074–0.7217) and the negative εNd(t) (-11.1 to -18.6) calculated at 1.03 Ga for pre-D2 granitoids and 0.95 Ga post-D2 granitoids (Fig. 13b) also imply that crustal protoliths were the source rocks for the granitoids, and preclude significant contributions from mantle-derived melts (Allègre and Ben Othman, 1988).

The anatectic gneisses in the GC sector plot in the field for greywacke in the litho-chemical classification diagrams (Basei et al., 2011) (Fig. 14c, d); the gneisses in the GC sector are thus considered to be majorly metagreywackes. The higher MgO abundances and the lower Fe# of the gneisses relative to the granitoids (Supplementary material[3], Table 2) suggest a restitic character for these gneisses. The mesocratic biotite ± hornblende gneisses

interleaved with minor amounts of garnet-free amphibolites are the dominant basement rocks exposed in the Godhra-Chhota Udepur sector, followed by the garnetiferous biotite-cordierite-sillimanite bearing melanocratic gneisses. In the granitoids, sporadic grains of mm-sized garnet porphyroblasts are noted only in a couple of outcrops, and sillimanite and cordierite are lacking. Assuming the gneisses continue to the depth where the granitoids originated, the mineralogical evidence and the geochemical signatures (Fig. 10–13) suggest that the mesocratic gneisses chemically resembling metagreywacke (Fig. 14) were the likely protolith for the S-type syn-collisional granitoids. The expansive granitoids are likely to have formed by partial melting via the model congruent melting reaction quartz + plagioclase + K-feldspar + biotite + garnet → melt (cf. Patiño Douce and Beard, 1996). The melting of the metagreywacke dominated protoliths (Vielzeuf and Schmidt, 2001) possibly occurred at 800–840 °C for the pink granitoids and 760–800 °C for the grey granitoids, inferred from zircon saturation temperature (T_{Zr}).

Based on the crystal-melt partition co-efficient of elements compiled by Rollinson and Pease (2021; Table 4.3 therein), the molar proportion of garnet in the model reaction should be small to account for the slight depletion of Y and HREEs in the granitoids relative to the gneisses; the enrichment of Nb, Ta, Th and U in the granitoids on the other hand precludes the involvement of Fe-Ti oxide phases (ilmenite) in the congruent melting reaction. Given the compatible nature of Nb (4–9.5) and Ta (1.2–1.9) (Rollinson and Pease, 2021), the modal proportion of biotite in the melting reaction is unlikely to be high. The Nb/Ta ratio is a measure of the degree of fractionation of the granitic magmas (Nb/Ta<5 indicating fractionation; Ballouard et al., 2016) whereas the Zr/Hf ratio is a measure of fertility of the magma in terms of metallogenic minerals like Sn, W, Mo, Be and Ta (Ballouard et al., 2016); the melts producing the GC granitoids were unfractionated (Fig. 10e) and “barren” in terms of metallic content (Fig. 10f) (Ballouard et al., 2016). The SMB and CGC granitoids also

show similar unfractionated and barren characteristics although the CGC granitoids originated as A-type magmas. S-type granites may exhibit geochemical characteristics similar to A-type granites (Whalen et al., 1987).

According to the Th/Ta versus Yb plot (Fig. 10g), these granitoids are from oceanic arcs and active continental settings. S-type granites are common in syn to post-collisional settings (Chappell and White, 2001; Sylvester, 1998). The syn-collisional nature of the granitoids is supported by the high-T deformation microstructures (Fig. 5f, g) and the magmatic flow textures (Fig. 4e) in these granitoids hosted within D3 shears. The field relations, the microstructures and the geochemical characteristics together suggest that the granitoids originated as a part of the Neoproterozoic accretion event in a syn-collisional setting. These granitoids are typical of the global Grenvillian-age felsic magmatism during Rodinia assembly (Chen et al., 2018).

5.3 ~2.5 Ga granitoids: the ADFB connection

A brief summary of the lithological, structural and chronological aspects of the Aravalli-Delhi Fold Belt is presented below to understand the Early Neoproterozoic accretion tectonics between the ADFB and the CITZ. The 700 km long N/NNE-striking Aravalli Delhi Fold Belt (ADFB) comprises Proterozoic Aravalli and Delhi supracrustal successions overlying an older basement referred to be the Banded Gneissic Complex (BGC) (Heron, 1953). The Archean nucleus in central and southern ADFB is known as BGC-I (Sharma, 2009). Archean granitoid bodies as in Untala, Gingla, Jagat, Berach and Ahar River areas, dated between 2.6 Ga and 2.4 Ga (Roy and Kroner, 1996; Wiedenbeck et al., 1996; Sivaraman and Odom, 1982; Kaur et al., 2019) constitute a major lithologic component in BGC-I. On the other hand, BGC-II is a more reworked component mantling the northern fringes of BGC-I (Sharma, 2009). BGC-II comprising the Sandmata-Mangalwar Complex

and the basement rocks underlying the Eastern Aravalli Terrane yield Late Paleoproterozoic dates, 1.8–1.75 Ga (Buick et al., 2006, 2010; Bhowmik et al., 2010; Kaur et al., 2019), deemed to represent the age of high-grade metamorphism in the ADFB. The poly-deformed Aravalli and Delhi Supergroups are Proterozoic in age (Bhowmik et al., 2010; Buick et al., 2006; 2010; D'Souza et al., 2019; Kaur et al., 2017; McKenzie et al., 2013). Archean dates obtained from detrital zircons in these rocks (Wang et al., 2017; D'Souza et al., 2019) suggest inherited components from an older basement.

The 2.5 Ga granitoids and gneisses are lacking in the CGC (Sequeira and Bhattacharya, 2021; Sequeira et al., 2020, 2021), in the southern and central domains of the SMB (Banerjee et al., 2021), and the southern part of the Godhra-Chhota Udepur sector (Fig. 7b). It appears, therefore, that the ~2.5 Ga granitoids in the northern domain of the Godhra-Chhota-Udepur sector correspond to the BGC-I ~2.5 Ga granitoids identified in several areas including Berach in the Aravalli-Delhi Fold Belt. These ~2.5 Ga foliated granitoids of the ADFB were tectonically juxtaposed with the Late Paleoproterozoic gneisses in the tectonic mélange in the GC sector (Fig. 2b). It is however unclear if the ~2.5 Ga granitoids occurred as tens-of meters to couple-of-hundreds of meters wide slivers inter-leaved with the 1.7–1.6 Ga anatectic gneisses of the CITZ or these granitoids (and gneisses) constitute tens-of-kilometre wide disparately evolved crustal segments juxtaposed with the Late Paleoproterozoic CITZ gneisses along the broken line in Fig. 2b. Nevertheless the gamut of evidence points to an accretion between the ADFB and the CITZ in the Godhra-Chhota Udepur sector. This accretion was contemporaneous with Early Neoproterozoic oblique D2-D3 crustal convergence (Banerjee et al., 2022a) and the coeval emplacement of 1.03–0.93 Ga S-type granites that originated by partial melting of sedimentary protoliths dominated by metagreywacke.

6. CONCLUSIONS

The gamut of evidence from field studies, LA-ICP-MS U-Pb (zircon) geochronology, chemical monazite dating and granite geochemistry indicates that the Archean (2.5–2.4 Ga) lithodemic units of the N/NNE-striking Aravalli-Delhi Fold Belt and the Late Paleoproterozoic (1.65–1.60 Ga) high-grade anatectic gneisses of the E-striking Central Indian Tectonic Zone were juxtaposed during oblique crustal accretion between the two terranes. The N-S crustal accretion involving top-to-the-south thrusting (D2 deformation) and nucleation of transpressional steep-dipping shear zones (D3 deformation) occurred between 1.03 and 0.93 Ga. Mesoscale structures (Figs. 2, 3 and 4) and deformation microstructures (Fig. 5) indicate that the D3 contractional deformation was broadly contemporaneous with the expansive emplacement of S-type syn-collisional granites formed by the partial melting of basement rocks dominated by metagreywacke, but the deformation outlasted the emplacement of the granitoids.

ACKNOWLEDGEMENTS

This work constitutes a part of the Doctoral dissertation of Anwesa Banerjee; the author acknowledges the financial support provided by the host Institute for her fellowship. The authors thank Ravikant Vadlamani (IIT Kharagpur) for helping with the whole rock Sm-Nd and Rb-Sr analyses, and his inputs in interpreting the data. N. Prabhakar (Department of Earth Sciences, IIT Bombay, India) kindly helped with X-ray element mapping and chemical dating of monazites. We acknowledge Debarun Dutta for his help in organising the fieldwork session at a difficult time during the pandemic. NS acknowledges the School of Earth, Ocean and Atmospheric Sciences, Goa University for permitting the collaborative work. The authors acknowledge the insightful comments of two anonymous journal reviewers; their comments went a long way in improving the clarity and presentation of the manuscript. The Editorial

handling of the manuscript and Editorial corrections by Greg Shellnutt are greatly appreciated.

APPENDIX

A. LA-ICP-MS U-Pb zircon dating

For separating zircons, the rocks were crushed, sieved and followed by panning to remove the lighter fractions. The heavier fractions were then passed through a column of bromoform to retrieve the heavy mineral fraction, and magnetic separation. The zircons were handpicked from the non-magnetic sample using a stereomicroscope. Araldite mounts were prepared for the embedded zircon grains; the mounts were polished to expose the internal structures of the grains.

The CL imaging of the zircon grains were done using the RELION CL instrument at the Plateforme GeOHeLiS, Géosciences Rennes, University of Rennes as well as with the Cameca SX-100 electron probe microanalyzer at the Department of Earth Sciences, Indian Institute of Technology Bombay, Mumbai. LA-ICP-MS U-Pb analyses of zircons were performed at the Plateforme GeOHeLiS, Géosciences Rennes, University of Rennes. A summary of instrumentation and analytical protocols are provided in Supplementary Material[4]. The analytical data for the zircon standard GJ-1 during the five analytical sessions is provided in the Supplementary Material[1]. The long-term uncertainty (1.9%) is only applied to population age and is quoted in italics between brackets in the text. All uncertainties are quoted at ± 2σ. Concordia diagrams are generated using IsoplotR (Vermeesch, 2018), and the reported MSWD are for concordance and equivalence.

No common Pb correction has been applied to the data as the measurement of ^{204}Pb is not precise enough on a Q-ICP-MS instrument. However, the presence of common lead has been qualitatively assessed using the f206c indicator which is calculated as follow:

$$f206c = (^{207}Pb/^{206}Pb_m - {}^{207}Pb/^{206}Pb^*)/(^{207}Pb/^{206}Pb_c - {}^{207}Pb/^{206}Pb^*)x100$$

where $^{207}Pb/^{206}Pbm$ is the measured ratio, $^{207}Pb/^{206}Pb^*$ is the radiogenic expected ratio given a defined age ($^{206}Pb/^{238}U$ age if it is < 1000 Ma, $^{207}Pb/^{206}Pb$ age if not) and $^{207}Pb/^{206}Pbc$ is the common Pb ratio based on the Stacey and Kramers (1975) Pb evolution model. As this factor relies on assumptions made on the age and on the Pb model it is only indicative, however we are confident that the data used for date calculation do not show high level of common Pb.

B. Monazite chemical dating

Monazite dating (Montel et al., 1996) was carried out in the Department of Earth Sciences, Indian Institute of Technology Bombay (Powai). The protocol for monazite analyses is detailed in Deshmukh et al. (2017) and only a brief summary is presented here. U–Th–total Pb monazite dating was performed using a CAMECA SX-FIVE electron probe microanalyzer (EPMA). Monazite analyses were determined with a 15 kV accelerating voltage, 200 nA beam current and 1 μm beam diameter. Pb M_a, Th M_a, and U M_b spectral lines were calibrated using crocoite ($PbCrO_4$), Th-glass (ThO_2 = 5 wt.%) and U-glass (UO_2 = 5 wt.%) standards, and were simultaneously measured in two LPET crystals for 240 s, 160 s, and 160 s, respectively. The peak and background intensities of Pb M_a, Th M_a, and U M_b were acquired with a five-cycle sub-counting methodology (Prabhakar, 2013; Deshmukh et al., 2017). The Pb M_a counts were determined using an exponential background fit to precisely define the distinctly located background positions (cf. Jercinovic and Williams, 2005; Spear et al., 2009). The matrix effects (ZAF) were reduced using the X-PHI approach (Merlet, 1992). The overlapping X-ray lines of Th M2-O4, Th Mζ1, Th Mζ2, YL_{C2}, YL_{C3}, La L_a on Pb M_a and Th M_c, Th M3-N4 on U M_b were corrected using the CAMECA Peak Sight software (version 6.1). Monazite dates were verified by analysing the Steenkampskraal monazite standard (SHRIMP age: 1030 ± 6 Ma; Knöper et al., 2000) during quantification.

Also, samples were chosen such that the abundances of the elements ThO_2 (2.96–20.65 wt%), UO_2 (0.01–1.72 wt%), PbO (0.19–0.83 wt%) and Y_2O_3 (0.5–3.09 wt%) were high to keep errors in background measurement low; only spots with 2σ errors <6% error [100x 2σ errors/total age in Ma] (Prabhakar, 2013) were considered. Based on X-ray element maps Th, U, Pb and Y (Fig. 6) and back-scattered electron images, 58 spot in chemically distinct domains were analyzed. The mean age population were statistically resolved using Isoplot 3.0 (Ludwig, 2012). Monazite analytical data and spot ages (±2σ errors) are presented in the Supplementary Material[2].

C. Whole rock major and trace element geochemistry

About 3-4 kg of rocks were broken into chips and crushed to less than 8 mm diameter in a Fritsch jaw crusher. The internal parts of the jaw crusher and the plastic collector was cleaned by ethyl alcohol and air dried before and after sample insertion. Sample contamination was avoided by flushing the channel by passing crushed rock chips and emptying the collector several times before starting the final crushing stage. After several rounds of cone and quartering, the representative fractions of the crushed rocks were powdered to less than 200mesh in a puck and ring Fritsch pulveriser. For the samples, at each step, both equipments were cleaned with water and soap, air dried, and wiped clean by ethyl alcohol. The samples were analyzed at ACME Lab, Bureau Veritas, Vancouver, Canada. Sample digestion was done by lithium borate fusion method. Analysis was done by Inductively Coupled Plasma Emission Spectrometry (ICP-ES) for major elements (package code: LF300), and Inductively Coupled Plasma Mass Spectrometer (ICP-MS) (package code: LF100) for trace elements. For the packages, the detection limits are 0.01 wt% for all major elements (detection limit is 0.002 wt% for Cr_2O_3). For trace elements, the detection limits are 0.01 to 0.1 ppm for REEs, 0.1–0.5 ppm for the other elements, except Ba , Be and Sn (1ppm) and V (8 ppm). The

analytical accuracy was controlled using the internal geological reference materials STD SO-19. The accuracy was better than ± 5%. The precision was verified by duplicated samples in each analytical set and the 2SD% (2SD/average*100) was also within ± 5%.

D. Sr and Nd isotope analysis

A set of seven granitoid samples were analysed to determine for Sr and Nd isotopic ratios at the Radiogenic Isotope Laboratory, IIT Kharagpur. The analysis was performed following protocols as in Mukherjee et al. (2019). About ~80 mg of whole rock powders (as in Appendix C) from each of the samples and one rock standard BCR2 (Columbia River Basalt, U.S. Geological Survey) were weighed, dissolved in screw capped Teflon vials with HF+HNO3 for three days and evaporated to bone dryness, followed by aqua regia attack steps for complete digestion. These digested samples were then evaporated to dryness and dissolved in 1M HCl and 0.1M HF solution for cation separation by ion exchange chromatography. Sr from the samples was eluted with 1.5 N HCl and LREE factions were collected in 6 N HCl on Teflon columns packed with 2mL BioRad AG50W x 8, 200e400 mesh cation exchange resin. All fractions were made to ~2 mL in 0.2% HNO3 to obtain <1mV background intensity for their respective pilot masses. Determination of isotope compositions was carried out in static mode on a Thermo Fisher Neptune Plus MC-ICPMS. Typical operating parameters during isotope measurement are given in the table:

MC- ICP conditions	
RF forward power	1200 W
Torch	Quartz torch
Sample gas flow	1.01 $Lmin^{-1}$
Auxiliary gas flow	0.8 L min^{-1}

Cool gas flow	16 L min^{-1}
Interface	
Sample cone	Nickel
Skimmer cone	Nickel
Data acquisitions conditions	
Wash (OPZ) meas. time	16 min (4-7 blocks of 10 cycles each)
Sampling meas. mode	20 min (6-10 blocks of 10 cycles each)
Integration time	4.194 s $cycle^{-1}$
Idle time	3 s

For Sr measurements, the isobaric interferences of Kr on ^{84}Sr and ^{86}Sr, and of Rb on ^{87}Sr were corrected using ^{83}Kr and ^{85}Rb, respectively; for correction of interfering ^{144}Sm on ^{144}Nd, both ^{147}Sm and ^{149}Sm were measured and ^{144}Nd corrected using an exponential law. Finally the blank On Peak Zero (OPZ) voltage intensities were subtracted from the sample intensities following the protocol of Thirlwall and Anczkiewicz (2004) for intensity correction. The isotope analysis per sample consisted of a single sequence measuring 8 blocks, with each block consisting of 10 cycles having an integration time of 4.194 s per cycle/sequence. The blank OPZ analyses consisted of 4 blocks, with 10 cycles per block. For IC measurements in samples, in-run mass bias was calculated from individual measurements using normalization to $^{88}Sr/^{86}Sr$ ratio = 8.37521 and $^{146}Nd/^{144}Nd$ = 0.7219 by exponential mass fractionation correction. The mass fractionation correction factors were calculated from the sample-standard bracketing method using 20210226 Sr standard for Sr and JNdi 20210302 standard (Tanaka et al., 2000) for Nd isotopes. The precision and accuracy of the data is checked on the reference material BCR-2 which was run along with the samples; values of $^{87}Sr/^{86}Sr$ =

0.70475±0.00006 (2σ) and $^{143}Nd/^{144}Nd$ = 0.512795±0.000030 (2σ) were obtained which is well within the accepted limits. For all calculations, ^{147}Sm-^{143}Nd decay constant ($\lambda = 6.54 \times 10^{-12}$ year^{-1}) is used after Lugmair and Marti (1978). The $\varepsilon_{Nd(T)}$ and Nd model ages (T_{DM}) were calculated using $^{143}Nd/^{144}Nd$ = 0.512630, $^{147}Sm/^{144}Nd$ = 0.1960 of CHUR (Bouvier et al., 2008) and for depleted mantle $^{143}Nd/^{144}Nd$ = 0.513151 and $^{147}Sm/^{144}Nd$ = 0.2136 (Goldstein and Jacobsen, 1988), respectively. The value for ^{87}Rb-^{86}Sr decay constant ($\lambda = 1.42 \times 10^{-11}$ year^{-1}) is used after Steiger and Jäger (1977).

Figure Captions

Figure 1: Generalized geological map of the northern part of India (see inset) showing the Great Indian Proterozoic Fold Belt (GIPFOB) in red dashes (modified from Banerjee et al., 2021, 2022a). The sub-domains of the GIPFOB namely the Aravalli Delhi Fold Belt (ADFB), the Satpura Mobile Belt (SMB) and the Chottanagpur Gneiss Complex (CGC) are marked. The CGC-SMB composite together constitute the Central Indian Tectonic Zone (CITZ). NIB, SIB and MC are the acronyms for the North India Block, the South India Block and the Marwar Craton respectively. The Godhra-Chhota Udepur sector is shown as rectangle in red at the southern tip of the Aravalli Delhi Fold Belt. Important cities shown are for reference only.

Figure 2: (a) Simplified lithological map of the Godhra-Chhota Udepur sector – compiled from District Resource Maps of the Geological Survey of India and modified from Banerjee et al. (2022a) – showing the major structural elements. The location of the Sanada granite pluton (Banerjee et al., 2022a) is shown. The bold black lines in the map represent the W-striking D3 mylonite zones; the white lines are the D3 sinistral shear zones and foliations. (b) Locations of samples used for geochronology and geochemistry (see later) are shown. The figure shows the spatial disposition of U-Pb

zircon dates for the 3 gneiss and 8 granitoid samples (this study, and Banerjee et al., 2022a). The sample locations (circled) and the corresponding concordant dates (bold), upper intercept (UI) and lower intercept (LI) Discordia dates are shown in comment boxes wherever applicable. Locations of samples used for monazite chemical dating, whole rock major and trace element geochemistry and whole rock Sr-Nd systematics used in this study are also shown. The different colors in the circles with the sample numbers pertain to the different types of analyses performed on the sample. The bold broken line is taken to separate the domains with ~2.5 Ga dates from the ~1.65 Ga dates. See section 3 for details.

Figure 3: (a) A 3-D block diagram depicting the litho-structural elements in the GC sector. The shallow-dipping D2 tectonic mélange is intersected by basement-piercing steep dipping, sinistral, transpressional D3 shear zones. Recumbent folds in the gneisses and the gently inclined folds in the supracrustal rocks are transposed into upright folds neighboring the steep-dipping D3 shears. The broadly collinear L2 and L3 stretching lineations, and NNE-striking and ENE-striking D4 conjugate shears are shown. (b–e) Lower hemisphere stereoplots of mesoscale structures in the basement gneisses, the supracrustal unit and the granitoids. Mesoscale structures corresponding with D2 are shown in (b-c) and for D3 are in (d-e). The stereoplots are modified from Banerjee et al. (2022a).

Figure 4: Field photographs showing mesoscale textures and structures of granitoids in the GC sector. The head of the marker pen (14 cm long) points to the north (N) for plan view images and to the top (T) for section view images. (a) Grey colored, massive (no mesoscale fabric), dynamically recrystallized (sugary appearance) granitoid with low abundance of ferromagnesian minerals (b) Shallow-dipping foliation (D2) defined by augen of K-feldspar phenocrysts and aggregates of biotite in blastoporphyritic foliated

granitoid. (c) Enclave of anatectic gneiss in a foliated porphyroblastic granitoid. Note that the steeply-dipping D3 protomylonite granite is intrusive into the gneiss that preserves a former D2 foliation. The fabric in the granitoid is axial planar to the open D3 folds in the gneiss; (d) Steeply-dipping granite mylonite in the D3 shear zone with oblique stretching lineations (e) S-C fabric showing sinistral kinematics in a deformed blastoporphyritic pink granitoid. Note K-feldspar phenocrysts are augen and recrystallized into a sugary white mosaic. (f) Blocky nature of the Godhra- granite. Note the sharp intrusive contact between the blastoporphyritic granitoid containing euhedral K-feldspar phenocrysts and the finer-grained granitoid devoid of phenocrysts (towards north).

Figure 5: Crossed polars photomicrographs of deformation microstructures in the pre-D2 granitoids (a–d) and the post-D2 granitoids (e–h). (a) Euhedral plagioclase grain in a medium-grained mosaic of dynamically recrystallized quartz and feldspars. Note the D2 fabric defined by shape preferred biotite aggregates wraps around the magmatic plagioclase grain. (b) Strain wavy xenoblastic lentils of quartz showing sub-grains and serrated grain and phase boundaries (arrow). (c) Medium-grained matrix comprising aggregates of dynamically recrystallized feldspar grains that are anchored to biotite flakes aligned defining the D2 fabric. (d) Weakly zoned (patchy) euhedral plagioclase grains show serrated margins against biotite flakes. (e) Part of a large microcline grains showing Carlsbad twinning; the adjacent quartz grains showing sub-grains and undulose extinction. (f) Trains and imbrications of euhedral plagioclase and microcline grains defining syn-D3 magmatic flow texture. Recrystallized quartz grain (in yellow in right centre, red arrow) shows chessboard sub-grain structure. (g) Chess-board sub-grain structure in quartz grains. (h) Intensely deformed post-D2 granitoid

exhibiting flaser texture in zone of high-D3 strain. Note the occurrence of quartz ribbons and the recrystallized nature of feldspars.

Figure 6: (a) Th/U versus $^{207}Pb/^{206}Pb$ age (in Ma) plot for analyzed zircon spots in granitoids and gneisses that yielded concordant ages. (b–j) Representative zircon cathodoluminescence (CL) images showing analyzed spots (circled) and corresponding $^{207}Pb/^{206}Pb$ ages with 2σ errors for the gneisses (b–c) and granitoids (d–j) in the Godhra-Chhota Udepur sector. The white circles represent concordant spots (>98% concordance); yellow circles pertain to discordant spots used to draw the Discordia.

Figure 7: U-Pb Concordia and Discordia plots for gneisses (a–b) and granitoids (c–i). In the Discordia plots (i) upper intercept (UI) ages and lower intercept (LI) ages with their 2σ errors are shown along with the MSWD. The total number of analyzed points (y) versus number of grain analyses used to define the Discordia (x) is also indicated as "n=x/y". The concordant points for each sample are plotted in (ii) and the number of concordant spots is "n". Green filled ellipses are the analyses kept for age calculations, while grey open ellipses are the discarded points.

Figure 8: Y and Th zoning maps and embedded spot dates (±2σ) in Ma of representative grains (two grains each) of analyzed monazite in AW-9B, 7, 163 and 12. Backscatter electron images (in shades of grey) correspond to the textural settings of the monazites. Probability-density plots show mean populations dates (in Ma with 2σ errors and MSWD) in monazites in the four samples: (a–b) anatectic gneiss (AW 9B), (c–d) anatectic gneiss (AW 7), (e–f) steeply foliated garnetiferous grey granitoid (AW 163) and (g–h) steeply foliated grey granitoid (AW 12). Acronyms used for minerals: plagioclase (P), K-feldspar (K), quartz (Q), muscovite/biotite (M/B). Monazites are circled.

Figure 9: (a) Probability-density plots for ^{207}Pb-^{206}Pb zircon ages (in granites and gneisses) and monazite chemical ages (in granitoids, gneisses and schists) in the Godhra-Chhota Udepur sector (this study; Banerjee et al., 2022a). The Pb-Pb zircon dates correspond to analyses with less than 2% discordance. The age peaks are shown with their 2σ errors and MSWD. "n" indicates the number of analyses used.

Figure 10: Geochemical plots and discrimination diagrams for the granitoids in the GC sector (data in Table 2). Square-shaped symbols are for pre-D2 granitoids, and diamonds are for post-D2 granitoids. The grey and pink fills in the symbols are for grey and pink granitoids respectively. (a) Total Alkali versus Silica (TAS) diagram with SiO_2 (wt%) versus Na_2O + K_2O (wt%). (b) molar $Al_2O_3/(Na_2O+K_2O)$ versus $Al_2O_3/(CaO+Na_2O+K_2O)$ plot. (c) ACF diagram for discriminating I and S-type granites (Yang et al., 2021); data for I and S-type granitoids from Lhasa block (Yang et al., 2021 and references therein) included for reference. (d) ΣREE versus $(Eu/Eu^*)_{CN}$ plot for the GC granitoids and gneisses. (e) Nb/Ta versus Ta plot after Ballouard et al. (2016); field shows the range of A-type granites after Ballouard et al. (2016); arrows show increasing fractionation trends suggested by the authors, e.g. trends with 10 wt.% biotite + 10 wt.% muscovite + 80 wt.% quartz indicated by dotted line; broken line is the trend with 10 wt.% biotite + 10 wt.% muscovite + 0.5 wt.% ilmenite + 79.5 wt.% (quartz + feldspar). (f) Nb/Ta versus Zr/Hf plots after Ballouard et al. (2016). Data for granitoids in CGC (Sequeira et al., 2021; Mukherjee et al., 2018) and SMB (Chattopadhyay et al., 2015, 2017) are added for comparison (e–g). (g) Th/Ta versus Yb after Gorton and Schandl, (2000).

Figure 11: Chondrite normalized REE patterns for (a) pink granitoids (b) grey granitoids and (c) gneisses in the GC sector (data in Table 2). The chondrite normalized (data from

McDonough and Sun, 1995) bulk crust composition (Rudnick and Gao, 2003) is plotted for comparison.

Figure 12: Bulk crust normalized (Rudnick and Gao, 2003) trace element patterns for (a) pink granitoids, (b) grey granitoids and (c) gneisses from the GC sector. An average gneiss composition calculated for the GC gneisses is shown with the bold blue line in (c). The GC average gneiss normalized trace element patterns for (d) pink granitoids and (e) grey granitoids.

Figure 13: Plots (data in Table 3) for GC sector granitoids. (a) $\epsilon_{Ndt=0}$ versus $^{87}Sr/^{86}Sr_{t=0}$ for all granitoids; (b) $\epsilon_{Ndt=1.03Ga}$ (pre-D2 granitoids) and $\epsilon_{Ndt=0.95Ga}$ (post-D2 granitoids) versus $^{87}Sr/^{86}Sr_i$. (c) $\epsilon_{Ndt=1.03Ga}$ (pre-D2 granitoids) and $\epsilon_{Ndt=0.95Ga}$ (post-D2 granitoids) versus T_{2DM}.

Figure 14: (a) Molar (Al_2O_3/MgO + FeO_T) versus molar (CaO/MgO + FeO_T) plot (after Altherr et al., 2000), and (b) Rb/Sr versus molar CaO/Na_2O diagram for the GC granitoids. Litho-chemical classification diagrams (after Basei et al., 2011) (c) log(Na_2O/K_2O) versus log (SiO_2/Al_2O_3) plot and (d) log (Fe_2O_3/K_2O) versus log (SiO_2/Al_2O_3) plot for gneisses of the GC sector. Legend for symbols are is in (c). Data in Table 2.

Table Captions

Table 1: Summary of lithology and mineral assemblage, morphology/texture of (a) zircon and (b) monazite, composition and dates in the 13 samples used for geochronology.

Table 1a: Summary of lithology and mineral assemblage, zircon morphology, Th/U ratio in zircon, and concordant and discordant dates. Isotope ratios and spotwise dates in zircons are in Supplementary Material[1].

Sample No.	Rock type and mineral assemblage	Zircon morphology	Number of analyzed grains and spots	Th/U ratios	Concordant and discordant dates (Ma) (±2σ)

AW 161	Gneiss	Quartzofeldspathic gneiss. D1 fabric defined by alternate layers of Hbl-Bt-Ms and Pl+Kfs-Qz; Rt, Opq and Zrn are accessory phases.	Zircon grains are long prismatic, width (80–100 µm), length (200–300 µm). The CL images exhibit core-rim textures; cores exhibit oscillatory or convolute zoning; rims appear to be recrystallized overgrowths (Fig. 6b).	23 grains/ 35 spots	0.04–1.60	Concordant date: 909 ± 11 (±36) Ma (MSWD: 0.51); Discordia dates: Upper intercept 2485 ± 15 (±96) Ma, Lower intercept 932 ± 15 (±39) Ma (MSWD: 1)
AW 114		Anatectic gneiss with alternate Hbl+Bt and Pl+Qz+Kfs layers; Rut, Zrn and Ilm are accessory phases.	Zircon grains are prismatic to square shaped; some prismatic grains are fragmented (Fig. 6c). Width (80–80 µm) and length (100 - 300 µm). CL images exhibit core-rim textures. The zircon cores mostly have a CL dark response, faint traces of oscillatory zoning is preserved in some of these cores. The rims on the zircon grains are overgrowths which have a bright CL response. Few grains are devoid of core-rim textures, are recrystallized, and have CL dark response.	24 grains/25 spots	0.04–1.25	Discordia dates: Upper intercept 1742 ± 20 (±69) Ma, Lower intercept 470 ± 30 (±35) Ma (MSWD: 0.41)
AW 18	Granitoids	Syn-D3 pink blastoporphyritic granitoid; Kfs+Pl+Qz+Bt; Sph, Zrn and Opq grains occur as accessory minerals.	Zircon grains are prismatic: width (60–100 µm), length (100–150 µm). In CL (Fig. 6d) the grains display well-defined oscillatory zoning; some of the grains have xenocrystic cores surrounded by new magmatic overgrowths.	15 grains/30 spots	0.3–1.91	Concordant date: 946 ± 6 (±37) Ma (MSWD: 0.54); Discordia dates: Upper intercept 955 ± 17 (±40) Ma, Lower Intercept 70 ± 68 (±69) Ma (MSWD: 0.43)

AW 145	Post-D2 blastoporphyritic granite; coarse grained rock comprising large (>1cm) grains of Kfs, Qz, Pl; Hbl+Bt+Ms occurs in subordinate amount; Zrn and Opq are accessory minerals.	Zircon grains are prismatic, wdt (50–80 µm) and length (100–150 µm). Magmatic oscillatory zoning observed in most grains in CL images (Fig. 6e), some grains exhibit overgrowth of homogenous metamorphic rim mantling magmatic cores.	19 grains/35 spots	0.37–2.52	Concordant date: 955 ± 7 (±37) Ma (MSWD: 1.2); Discordia dates: Upper intercept 2525 ± 46 (±106) Ma, Lower Intercept 944 ± 15 (± 39) Ma (MSWD: 1)
AW 98	D3 blastoporphyritic granite comprising large grains Qz lentils and Kfs in a fine-grained mosaic of Qz+Kfs+Pl+Ms; Hbl and Bt occur as accessory phase along with Zrn and Fe-Oxide minerals	Zircon grains are long prismatic; width (60–80 µm) and length (150–300 µm). The grains exhibit magmatic oscillatory zoned cores with homogenous metamorphic overgrowths; in a few grains the core exhibits convolute zoning (Fig. 6f).	14 grains/30 spots	0.09–1.82	No alignment on Wetherill Concordia diagram
AW 127	D3 pegmatoidal granitoid with end-to-end touching imbricate Kfs grains (>6cm long) showing Carlbad twins. Kfs grains are euhedral to subhedral, Pl grains are weakly zoned; feldspars are weakly recrystallized.	Zircon grains are long prismatic; width (80–120 µm) and length (200–300 µm). The grains exhibit magmatic oscillatory zoning in CL images (Fig. 6g). A few grains also show recrystallization textures and generally have CL dark response.	21 grains/25 spots	0.22–1.41	Concordant date: 951 ± 10 (±37) Ma (MSWD:1.2)
AW 9A	Coarse-grained post-D2 granitoid comprising majorly Qz-Kfs-Pl and Bt; Zrn, Ap, and opaque minerals occur as accessory phases; randomly oriented retrograde muscovite is associated with Kfs	Zircon grains are prismatic; while some grains are long and slender others are short and stout as is evident from their length to width ratios of 4–5 and 1.2–1.6 respectively. The cores of these zircon grains are completely recrystallized and have a CL dark response which is surrounded by oscillatory zoned overgrowths in some cases (Fig. 6h); in other grains the rims are	13 grains/30 spots	0.09–1.82	Discordia dates: Upper Intercept 2544 ± 82 (±127) Ma, Lower Intercept 958 ± 26 (±45) Ma (MSWD: 0.88)

		homogenous and have a CL bright response (Fig. 6h).			
AW 73	Pre-D2 blastoporphyritic granitoid comprising Kfs-Pl-Qz-Bt-Hbl-Ms; Zrn and Opq minerals occurs as accessory phases	Zircon grains are prismatic; width (40–80 µm), length (100–300 µm). The grains exhibit core-rim texture in CL images; the cores have CL dark and bright responses, the rims bear oscillatory zoning indicative of magmatic overgrowths.	18 grains/40 spots	0.08–1.08	Discordia dates: Upper Intercept 1026 ± 17 (±43) Ma, Lower Intercept 111 ± 40 (±40) Ma (MSWD: 1.4) Concordant date: 983 ± 11 (±39) Ma (MSWD: 1.4);
AW 8	Pre-D2 granitoid, relatively fine-grained, comprising Kfs+Pl+Qz+Bt+Hb+Ms; Zrn-occurs as accessory phase	The zircon grains are short prismatic to rectangular shaped; length to width ratio varying from 1.5–2. Some grains exhibit core-rim textures in CL, others are concentrically zoned.	22 grains/40 spots	0.07–1.80	Discordia dates: Upper Intercept 1020 ± 22 (±45) Ma, Lower Intercept 186 ± 35 (±36) Ma (MSWD: 0.95)

Table 1b: Brief summary of lithology, mineral assemblage and summary of monazite textures, composition and chemical dates. Spot wise chemical composition, age, and 2σ errors (in Ma) of monazites are provided in Supplementary Material[2].

Sample No.		Rock type and mineral assemblage	Textural setting of monazites	Zoning pattern and chemical variations in monazites	No. of analyzed grains and spots	Range of spot dates (±2σ) and mean dates (±2σ) in Ma
AW 9B	**Gneiss**	Basement anatectic gneiss comprising coarse-grained mosaic of Kfs-Qz-Pl-Bt-Hbl; calcite veins occur in the rock at places. Mnz is accessory mineral	Rounded to short prismatic grains of 60–80 µm (long axes)occur associated with Bt	Zoning is patchy-nebulous. ThO_2 (5.37–12.64 wt%), UO_2 (0.01–0.65 wt%), PbO (0.25–0.59), Y_2O_3	3 grains/ 11 spots	878 ± 28 to 940 ±38 Ma; 923 ± 13 (MSWD:1.8)

				(0.50–2.48)		
AW 7		Coarse grained quartzofeldspathic gneiss (Kfs-Pl-Qz-Ms-Bt); Cpx occurs as an accessory phase with Hbl, Chl and Mnz.	Long and short prismatic grains of 60–100 µm (long axes); occur associated with the Bt grain aggregates	Zoning is patchy-nebulous. ThO_2 (6.06–9.70 wt%), UO_2 (0.14–1.69 wt%), PbO (0.23–0.62), Y_2O_3 (1.11–2.62)	5 grains/ 14 spots	876 ± 26 to 1020 ± 32 Ma; 911 ± 22 (MSWD: 7.1)
AW 163	Granitoids	Post D2 granitoid with fine grained mosaic of Bt-Ms-Hb-Qz-Pl-Kfs-Grt. Zrn-Rt-Mnz-Opq occur as accessory phases.	Short prismatic grains with long axis >50 µm; associated with foliated Bt, and also in the recrystallized quartz-feldspar mosaic.	Zoning is patchy-nebulous; rarely concentric. ThO_2 (2.96–10.64 wt%), UO_2 (0.24–1.25 wt%), PbO (0.21–0.47), Y_2O_3 (1.69–3.09)	5 grains/ 12 spots	872 ± 47 to 959 ± 27 Ma; 908 ± 19 (MSWD: 2.7)
AW 12		Post-D2 blastoporphyritic granitoid comprising Bt-Ms-Kfs-Qz-Pl assemblage. Mnz is an accessory phase.	Sub-rounded to elliptical grains (long axis 100–150 µm) occur within aggregates/individual Bt grains; monazite exhibits no preferred alignment	Zoning is patchy-nebulous. ThO_2 (4.48–14.07 wt%), UO_2 (0.15–1.02 wt%), PbO (0.19–0.83), Y_2O_3 (0.88–2.56)	5 grains/ 21 spots	863 ± 50 to 969 ± 47 Ma; 926 ± 11 (MSWD: 3.3)

Mineral abbreviations: Biotite (Bt), chlorite (Chl), garnet (Grt), hornblende (Hb), ilmenite (Ilm), K-feldspar (Kfs), monazite (Mnz), muscovite (Ms), opaque phase (Opq); plagioclase (Pl), quartz (Qtz); rutile (Rt), zircon (Zrn).

Table 2: Major and trace element compositions of granitoids and gneisses in the GC sector.

	Pink Granitoids										**Grey Granitoids**										**Gneiss**				
	pre-D2		**post-D2**								**pre-D2**		**post-D2**												
Sample	**AW-1**	**AW-5**	**AW-18**	**AW-21**	**AW-98**	**AW-10**	**AW-127**	**AW-145**	**AW-155**		**AW-8**	**AW-73**	**AW-14**	**AW-15**	**AW-16**	**AW-38**	**AW-63**	**AW-11A**	**AW-77A**	**AW-9A**	**AW-7**	**AW-11B**	**AW-22**	**AW-161**	**AW-142B**
SiO_2	74.7	67.5	67.9	69.0	71.3	72.4	68.8	75.7	55.2		71.9	72.1	63.3	68.7	71.9	66.5	76.0	73.4	73.1	73.4	68.9	71.3	69.7	59.9	61.6

Al_2O_3	13.8	15.0	14.3	16.4	14.4	13.4	13.7	11.9	17.7	14.0	14.2	15.0	15.0	14.3	15.5	10.2	13.9	14.1	14.3	13.8	12.2	14.0	15.7	16.2
Fe_2O_3	1.50	3.76	3.84	1.70	2.66	2.79	3.92	2.07	6.55	2.09	2.12	6.17	3.38	2.00	3.51	1.67	1.42	1.66	0.54	4.78	3.93	3.21	7.12	8.36
FeO	1.35	3.38	3.45	1.53	2.39	2.51	3.53	1.86	5.89	1.88	1.91	5.55	3.04	1.80	3.16	1.50	1.28	1.49	0.49	4.30	3.54	2.89	6.41	7.52
MgO	0.38	0.90	1.36	0.69	0.42	0.42	1.26	0.32	2.87	0.36	0.38	1.82	1.99	1.46	1.25	1.25	0.23	0.30	0.18	2.06	1.54	2.17	2.82	3.96
CaO	0.24	2.07	2.49	3.31	1.50	1.13	1.95	0.60	4.76	1.10	1.40	2.86	1.84	1.41	2.83	1.51	0.87	1.17	1.02	1.39	0.34	2.35	3.76	0.95
Na_2O	4.80	3.50	3.20	4.17	3.34	3.00	2.68	2.40	3.61	2.88	3.47	3.10	2.90	3.06	3.37	0.68	3.34	3.33	2.51	3.45	1.20	4.00	4.17	0.82
K_2O	2.59	4.62	4.44	2.73	2.24	5.12	4.94	5.87	5.42	5.79	4.94	4.53	5.03	5.28	4.18	4.89	5.27	5.10	6.88	2.84	7.56	2.26	3.72	4.36
TiO_2	0.21	0.58	0.60	0.20	0.24	0.26	0.53	0.18	1.00	0.26	0.26	1.22	0.30	0.28	0.59	0.14	0.17	0.19	0.06	0.65	0.53	0.47	0.93	0.75
P_2O_5	0.05	0.28	0.27	0.09	0.07	0.13	0.24	0.03	0.67	0.06	0.09	0.45	0.17	0.12	0.16	0.06	0.06	0.08	0.06	0.20	0.21	0.10	0.61	0.27
MnO	0.03	0.05	0.06	0.05	0.04	0.06	0.06	0.02	0.09	0.02	0.04	0.08	0.04	0.03	0.04	0.04	0.03	0.03	bdl	0.04	0.05	0.05	0.09	0.06
Cr_2O_3	bdl	bdl	0.01	bdl	bdl	bdl	bdl	bdl	0.01	bdl	bdl	0.01	bdl	bdl	0.01	bdl	bdl	bdl	bdl	0.01	0.01	0.01	bdl	0.01
LOI	1.50	1.30	1.10	1.30	1.50	1.00	1.40	0.40	1.30	1.10	0.60	1.00	1.10	0.90	1.60	3.30	1.00	0.70	0.70	1.60	0.80	1.30	0.80	2.30
Sum	99.8	99.8	99.8	99.9	99.8	99.8	99.8	99.7	99.8	99.7	99.8	99.7	99.8	99.8	99.8	99.8	99.8	99.8	99.8	99.8	99.8	99.8	99.8	99.8
A/CNK	1.24	1.03	0.98	1.04	1.12	1.07	1.03	1.04	0.86	1.07	1.05	0.99	1.11	1.07	1.02	1.11	1.09	1.08	1.07	1.02	1.21	1.17	0.72	0.71
Fe#	0.67	0.68	0.59	0.55	0.76	0.77	0.61	0.77	0.54	0.75	0.74	0.63	0.63	0.69	0.59	0.40	0.76	0.74	0.60	0.38	0.07	0.47	0.36	0.09
Be	4.00	3.00	2.00	3.00	2.00	3.00	4.00	2.00	2.00	3.00	4.00	2.00	3.00	5.00	4.00	bdl	5.00	3.00	1.00	5.00	2.00	5.00	5.00	bdl

Sc	3.00	5.00	9.00	4.00	5.00	30.00	10.00	2.00	14.00	5.00	5.00	11.0	7.00	4.00	8.00	4.00	3.00	4.00	2.00	11.0	9.00	9.00	13.0	20.0
V	18.0	41.0	53.0	22.0	19.0	18.0	54.0	11.0	112.0	13.0	18.0	81.0	43.0	20.0	60.0	38.0	11.0	13.0	13.0	53.0	48.0	39.0	125.0	146.00
Co	74.4	83.4	118.6	74.8	82.4	136.6	91.2	161.3	57.0	159.4	131.5	89.4	112.3	120.9	101.5	80.4	85.8	115.0	142.3	77.5	106.7	115.5	89.6	141.50
Ni	bdl	bdl	bdl	bdl	bdl	bdl	bdl	bdl	26.00	bdl	bdl	bdl	bdl	bdl	bdl	bdl	bdl	bdl	bdl	21.0	26.0	65.0	32.0	34.00
Ga	20.2	18.4	17.5	15.3	20.9	17.3	16.7	18.7	20.5	17.0	19.9	20.1	18.4	20.7	21.1	8.6	18.7	19.2	13.8	16.6	13.5	19.8	23.0	22.60
Rb	97.2	156.8	182.9	87.5	183.1	250.8	172.9	162.8	113.8	232.0	251.7	152.5	224.1	272.2	147.5	111.8	217.6	301.1	235.3	140.4	334.2	129.8	165.2	233.4
Sr	44.7	377.8	323.5	528.1	97.6	114.0	444.1	190.3	1479.2	128.5	119.4	366.2	232.5	144.1	671.6	100.4	135.6	113.3	119.4	79.4	74.6	206.9	597.4	53.2
Y	63.8	24.4	27.6	19.60	22.1	46.5	25.8	12.4	31.1	11.0	15.0	30.9	19.3	13.4	17.9	4.9	13.2	27.5	10.3	31.0	22.5	10.1	24.6	26.4
Zr	249.5	445.2	311.6	100.3	230.3	271.5	371.7	502.2	674.0	246.8	228.0	540.7	229.1	198.9	233.6	78.4	133.5	162.4	121.3	376.0	377.1	437.2	330.8	176.4
Nb	20.50	14.80	20.30	6.60	17.70	16.00	17.00	8.70	17.90	14.9	23.3	32.4	14.2	15.5	10.7	3.40	13.4	17.3	3.10	14.6	11.0	16.1	12.9	13.1
Sn	5.00	4.00	3.00	bdl	5.00	3.00	2.00	2.00	2.00	bdl	6.00	2.00	2.00	5.00	2.00	bdl	2.00	5.00	bdl	2.00	2.00	2.00	2.00	2.00
Cs	1.20	1.60	5.10	2.50	1.00	4.80	2.60	1.50	1.10	2.60	3.90	2.00	4.20	7.20	3.10	1.50	5.40	6.90	4.10	5.90	4.80	3.80	1.40	10.10
Ba	195	1356	882	1108	414	642	1416	1073	3100	741	653	1472	988	640	1485	1259	724	508	558	248	1240	468	1108	434
La	100.8	184.6	110.2	27.6	97.8	79.6	212.3	63.1	277.1	117.5	75.5	101.1	72.8	79.0	67.2	22.9	39.7	64.1	33.1	55.4	48.5	25.8	93.6	64.4
Ce	160	329	187	47.	205	144	360.	115.	466.	201	144	187	132	150	118	37.	66.8	117.	54.	106	93.4	46.	179.	117.

	.8	.0	.6	6	.5	.7	2	8	1	.8	.7	.0	.2	.0	.3	7		1	5	.3		4	6	8
Pr	23.5	32.9	20.4	5.1	19.7	15.4	35.3	12.4	49.3	20.5	14.4	20.2	14.4	16.0	12.5	3.8	7.2	11.8	5.7	11.2	9.8	5.1	21.2	13.1
Nd	85.3	104.5	68.6	18.1	64.0	52.5	110.0	43.3	162.1	64.1	46.0	70.7	50.1	52.6	42.3	12.8	23.7	39.6	18.8	39.1	34.0	18.6	75.8	46.5
Sm	14.56	13.96	10.11	2.83	10.09	9.55	13.75	6.58	21.59	8.71	7.03	10.82	7.47	8.24	6.00	1.95	4.10	6.27	2.90	7.15	6.29	3.12	12.01	8.53
Eu	0.34	1.57	1.43	0.65	0.77	0.87	2.29	0.71	4.49	0.88	0.73	2.12	1.33	0.89	1.23	0.54	0.61	0.64	0.66	1.37	1.24	1.09	2.21	1.57
Gd	12.82	8.86	7.18	2.01	7.01	9.38	8.56	4.61	12.63	5.20	4.99	8.44	5.35	4.93	4.20	1.38	3.18	5.04	2.23	6.36	5.37	2.70	8.39	7.35
Tb	1.90	1.10	0.96	0.29	0.94	1.57	1.07	0.58	1.45	0.54	0.64	1.12	0.71	0.58	0.55	0.19	0.43	0.75	0.33	0.96	0.76	0.34	0.98	1.02
Dy	11.06	5.34	5.11	1.60	4.73	9.36	5.19	2.67	6.69	2.31	3.25	5.90	3.63	2.69	3.09	0.99	2.49	4.41	1.75	5.75	4.39	1.96	4.87	5.60
Ho	2.23	0.92	0.93	0.32	0.78	1.89	0.91	0.46	1.12	0.35	0.54	1.11	0.69	0.44	0.58	0.19	0.48	0.93	0.37	1.13	0.86	0.37	0.85	0.94
Er	6.27	2.20	2.64	0.93	1.95	5.02	2.56	1.17	2.67	0.94	1.40	3.06	1.87	1.22	1.73	0.58	1.34	2.69	0.95	3.25	2.48	1.02	2.25	2.41
Tm	0.94	0.31	0.40	0.14	0.26	0.67	0.36	0.17	0.39	0.13	0.17	0.42	0.26	0.17	0.25	0.07	0.19	0.39	0.14	0.45	0.33	0.15	0.31	0.27
Yb	6.14	2.03	2.48	0.99	1.57	4.03	2.34	1.34	2.39	0.90	1.06	2.79	1.70	1.14	1.66	0.55	1.42	2.64	1.08	3.06	2.13	1.09	2.01	1.63
Lu	0.90	0.32	0.37	0.16	0.23	0.57	0.34	0.24	0.35	0.13	0.15	0.43	0.26	0.17	0.22	0.08	0.22	0.38	0.15	0.44	0.34	0.19	0.29	0.24
Hf	7.20	10.20	7.70	2.70	6.60	7.80	9.20	12.90	16.60	7.20	6.40	12.30	6.00	5.90	6.20	2.10	4.10	4.90	3.30	10.20	10.30	11.40	7.80	5.10
Ta	1.80	1.10	1.70	0.60	1.80	1.20	1.10	0.60	1.00	0.80	2.40	1.50	1.10	1.90	1.40	0.50	1.70	2.70	0.60	1.50	1.00	0.90	0.60	1.20
W	552.	711.	842.	647.	527.	1063	669.5	1210.	346.3	1125	971.	658.	674.	916.	739.	723.	803.5	814.3	929.	593.	694.9	838.	492.6	924.6

Th	5 35.1	9 38.1	5 38.3	8 14.1	0 62.0	.5 32.7	49.0	8 24.4	71.3	.6 63.4	7 34.6	5 19.3	1 37.9	7 46.1	4 29.1	2 12.3	19.9	44.5	3 29.2	0 39.7	26.0	0 8.6	12.4	26.4			
U	6.80	3.20	4.80	1.90	6.10	2.70	2.60	4.80	2.60	5.70	4.20	2.10	4.30	4.10	4.40	1.30	2.60	6.20	10.70	6.00	5.50	2.70	1.10	3.50			
ΣREE	427.5	687.6	418.4	108.3	415.3	335.1	755.2	253.1	1008.4	424.0	300.5	415.3	292.8	318.0	259.9	83.7	151.8	256.8	1222.6	241.9	209.9	107.9	404.3	271.4			
Eu/Eu*	0.08	0.43	0.51	0.83	0.28	0.28	0.64	0.39	0.83	0.40	0.38	0.68	0.64	0.43	0.75	1.00	0.31	0.35	0.79	0.62	0.65	1.14	0.67	0.60			
TZrWH88	846	872	731	741	824	836	859	900	854	827	817	799	818	700	676	741	775	791	765								
TZrB13	819	836	786	865	787	798	823	878	790	788	775	739	764	776	758	693	729	746	717								

bdl: below detection limit
A/CNK=molar AL2O3/CaO+Na2O+K2O
Fe#=molar FeO/FeO+MgO
Eu/Eu*=$Eu_N/\sqrt{(Sm_N*Gd_N)}$
WH88: Watson and Harrison, 1988; B13: Boehnke et al., 2013

Table 3: Whole rock Sr and Nd isotopic data for granitoid samples from the GC sector.

Sample	Granite type		87Sr/86Sr	Sm (ppm)	Nd (ppm)	147Sm/144Nd	143Nd/144Nd	T DM	T 2DM	T CHUR	f(Sm/Nd)	εNd (0)	εNd (T)	Time T (Ma)
AW5	Pink Granite	pre D2	0.7322	13.96	104.5	0.0841	0.511407	2.05E+09	2.43E+09	1.65E+09	-0.6	-23.9	-11.1	1030
AW21	Pink Granite	post D2	0.7156	2.83	18.1	0.0985	0.511318	2.42E+09	2.75E+09	2.03E+09	-0.5	-25.6	-13.7	950
AW127	Pink Granite	post D2	0.7231	13.75	110	0.0787	0.511110	2.30E+09	2.89E+09	1.96E+09	-0.6	-29.7	-15.4	950
AW145	Pink Granite	post D2	0.7562	6.58	43.3	0.0957	0.511318	2.36E+09	2.72E+09	1.97E+09	-0.5	-25.6	-13.4	950
AW8	Grey Granite	pre D2	0.7889	8.71	64.1	0.0856	0.511033	2.51E+09	3.05E+09	2.18E+09	-0.6	-31.2	-18.6	1030
AW16	Grey Granite	post D2	0.7910	8.24	52.6	0.0987	0.511235	2.53E+09	2.89E+09	2.16E+09	-0.5	-27.2	-15.4	950
AW38	Grey Granite	post D2	0.7185	6.00	42.3	0.0893	0.511281	2.28E+09	2.72E+09	1.91E+09	-0.5	-26.3	-13.3	950

$^{143}Nd/^{144}Nd=0.512630$, $^{147}Sm/^{144}Nd=0.1960$ of CHUR (Bouvier et al., 2008)
$^{143}Nd/^{144}Nd=0.513151$, $^{147}Sm/^{144}Nd=0.2136$ of Depleted Mantle (DM) (Goldstein and Jacobsen, 1988)
$\lambda^{147}Sm= 6.54*10^{-12}yr^{-1}$ (Lugmair and Marti, 1978)
$\lambda^{87}Rb= 1.42*10^{-11}yr^{-1}$ (Steiger and Jäger, 1977))

Deformation events	**Basement gneiss (autochthonous)**	**Granitoids**	**Supracrustal Unit (allochthonous)**	**Tectonic significance**	**U-Pb zircon and monazite ages**

Abbreviations: CHUR=Chondrite Uniform Reservoir, DM= Depleted Mantle

Table 4: Summary of pre-D2, D2 and D3 deformation features, age and tectonic significances in the three lithodemic units, e.g. the basement gneisses, the supracrustal unit, and pre- and post-D2 granitoids.

Pre-D2	Granulite facies anatectic metamorphism manifested by two high-temperature fabrics D1a and D1b	Post-D1a, b granitoids intrusive into the anatectic basement gneisses; older granitoids do not share the D1a,b fabrics in the gneisses.	Recumbent isoclinal folds on colour banding (S0) in the supracrustal unit, with the development of penetrative S1 fabric at greenschist-epidote amphibolite facies.	The high temperature anatectic event in the gneisses is not reflected in the supracrustal unit. Similarly, the high-T D1a, b events in the gneisses are not shared by the pre-D2 granitoids.	High-grade metamorphism in gneisses occurred at 1.7–1.6 Ga. Pre-D2 granitoids belong to two age clusters, e.g. 2.5–2.4 Ga, and 1.03–1.02 Ga.
D2	Recumbent folds developed on anatectic layers in gneisses with gentle WNW plunging fold axes; pervasive axial plane fabric not observed	Pre-D2 granitoids develop shallow dipping mylonitic foliation (S2) with WNW plunging stretching lineations (L2)	Recumbent D2 folds develop on S0-S1 fabrics in the allochthonous supracrustal rocks; the deformation produces gently dipping axial planes (S2) and WNW gently plunging fold axes (L2)	Overthrusting (top-to-the-south) of the allochthonous supracrustal unit over the gneiss-granitoid basement due to N-S shortening	This deformation post-dates the emplacement of~1.03–1.02 Ga, and juxtaposes the 2.5–2.4 Ga granites with the 1.7–1.6 Ga gneisses, and low-grade supracrustal rocks.
D3	Upright folds on D2 recumbent folds of D1a-D1b gneissic layers in anatectic gneisses. The WNW plunging gentle to moderately plunging folds do not possess pervasive axial plane fabric	Post-D2 to syn-D3 granitoid emplacements; these D3 granitoids exhibit steep dipping mylonitic foliation (S3) with moderate WNW plunging stretching lineations (L3) in vicinity of D3 shears.	Moderately plunging upright folds on D2 recumbent folds and shallow-dipping phengite-chlorite S2 axial planes in micaceous rocks in the supracrustal unit, at the vicinity of E-striking D3 shears with E-W striking axial planes (S3) and WNW moderately plunging fold axes (L3)	Progressive N-S shortening led to a switchover from the thrust regime (D2) to a wrench dominated deformation (D3) involving flipping of Z strain axes from vertical to horizontal for the same E-W orogen parallel stretching; this led to nucleation of	~0.95–0.93 Ga age of post D2 to syn D3 granitoids, and the 1.03 Ga pre-D2 granitoids thus constrain the D2-D3 crustal convergence between 1.03–0.93 Ga.

		E-W striking, basement piercing, steep dipping, sinistral, transpressional D3 shear zones

Supplementary Materials

Supplementary Material[1]: U-Pb zircon analytical data for gneisses (AW161, AW 114) and granitoids (AW 18, AW 145, AW 127, AW 98, AW 3A, AW 73, AW 8) from the Godhra-Chhota Udepur sector. Lines in bold and italics are discordant analyses, lines in bold are concordant analyses. Analytical data for quality control material GJ-1 is also provided.

Supplementary Material[2]: Electron probe microanalytical data of monazites, spot ages with 2σ errors in Ma, and error % computed following Prabhakar (2013).

Supplementary material[3]: Harker variation diagrams for the major element oxides (a) Al_2O_3 (b) Fe_2O_3 (c) MgO (d) CaO (e) K_2O (f) Na_2O (g) molar FeO/(FeO+MgO) and (h) ΣREE versus SiO_2 (wt%) for granitoids and gneisses of the GC sector.

Supplementary Material[4]: Summary of instrumentation and analytical protocols for the LA-ICP-MS equipment used for LA-ICP-MS U-Pb zircon dating

REFERENCES

Allègre, C. J., Ben Othman, D., 1980. Nd–Sr isotopic relationship in granitoid rocks and continental crust development: a chemical approach to orogenesis. Nature 286, 335–342.

Altherr, R., Holl, A., Hegner, E., Langer, C., Kreuzer, H., 2000. High-potassium, calc-alkaline I-type plutonism in the European Variscides: northern Vosges (France) and northern Schwarzwald (Germany). Lithos 50, 51–73.

Ballouard, C., Poujol, M., Boulvais, P., Branquet, Y., Tartèse, R., Vigneresse, J. L., 2016. Nb-Ta fractionation in peraluminous granites: A marker of the magmatic-hydrothermal transition. Geology 44, 231–234. https://doi.org/10.1130/G37475.1

Banerjee, A., Sequeira, N., Bhattacharya, A., 2021. Tectonics of the Greater India Proterozoic Fold Belt, with emphasis on the nature of curvature of the belt in west-central India. Earth Science Reviews, 221, 103758. https://doi.org/10.1016/j.earscirev.2021.103758

Banerjee, A., Sequeira, N., Naraga, P., Cogné, N., Bhattacharya, A., 2022a. Early Neoproterozoic tectonics in the Godhra – Chhota Udepur sector: Evidence for two-stage accretion in the Greater India Proterozoic Fold Belt (GIPFOB). Lithosphere https://doi.org/10.2113/2022/9322892.

Banerjee, A., Prabhakar, N., Sequeira, N., Cogné, N., Battacharya, A., 2022b. Dynamics of Early Neoproterozoic accretion, west-central India: II Early Neoproterozoic LT-HP and Early Paleoproterozoic HT-LP metamorphism at Godhra-Chhota Udepur, and a tectonic model for accretion. Lithos (Accompanying article: being revised).

Basei, M. A. S., Drukas, C. O. Nutman, A. P., Wemmer, K., Dunyi, L., Santos, P. R., Passarelli, C. R., Campos Neto, M. C., Siga Jr, O., Osako, L., 2011. The Itajaı´ foreland basin: a tectono-sedimentary record of the Ediacaran period, Southern Brazil. International Journal of Earth Science 100, 543–569.

Bhowmik, S.K., Bernhardt, H.J., Dasgupta, S., 2010. Grenvillian age high-pressure upper amphibolite-granulite metamorphism in the Aravalli-Delhi Mobile Belt, Northwestern India: New evidence from monazite chemical age and its implication. Precambrian Research 178, 168–184. https://doi.org/10.1016/j.precamres.2010.02.015

Boehnke, P., Watson, E. B., Trail, D., Harrison, T. M., Schmitt, A. K., 2013. Zircon saturation re-revisited. Chemical Geology 351, 324–334. https://doi.org/10.1016/j.chemgeo.2013.05.028

Bouvier, A., Vervoort, J. D., Patchett, P. J., 2008. The Lu–Hf and Sm–Nd isotopic composition of CHUR: constraints from unequilibrated chondrites and implications for the bulk composition of terrestrial planets. Earth and Planetary Science Letters 273, 48–57.

Buick, I.S., Allen, C., Pandit, M., Rubatto, D., Hermann, J., 2006. The Proterozoic magmatic and metamorphic history of the Banded Gneiss Complex, central Rajasthan, India: LA-ICP-MS U-Pb zircon constraints. Precambrian Research 151, 119–142. https://doi.org/10.1016/j.precamres.2006.08.006

Buick, I.S., Clark, C., Rubatto, D., Hermann, J., Pandit, M., Hand, M., 2010. Constraints on the Proterozoic evolution of the Aravalli–Delhi Orogenic belt (NW India) from monazite geochronology and mineral trace element geochemistry. Lithos 120, 511–528. https://doi.org/10.1016/j.lithos.2010.09.011

Chappell, B. W., White, A. J., 2001. Two contrasting granite types: 25 years later. Australian Journal of Earth Sciences, 48, 489–499.

Chattopadhyay, A., Das, K., Hayasaka, Y., Sarkar, A., 2015. Syn-and post-tectonic granite plutonism in the Sausar Fold Belt, central India: age constraints and tectonic implications. Journal of Asian Earth Sciences 107, 110–121. https://doi.org/10.1016/j.jseaes.2015.04.006

Chattopadhyay, A., Chatterjee, A., Das, K., Sarkar, A., 2017. Neoproterozoic transpression and granite magmatism in the Gavilgarh-Tan Shear Zone, central India: Tectonic significance of U-Pb zircon and U-Th-total Pb monazite ages. Journal of Asian Earth Sciences 147, 485–501. https://doi.org/10.1016/j.jseaes.2017.08.018

Chen, W. T., Sun, W. H., Zhou, M. F., Wang, W., 2018. Ca. 1050 Ma intra-continental rift-related A-type felsic rocks in the southwestern Yangtze Block, South China. Precambrian Research 309, 22–44.

Clemens, J. D., 2003. S-type granitic magmas—petrogenetic issues, models and evidence. Earth Science Reviews 61, 1–18.

Clemens, J. D., Helps, P. A., Stevens, G., 2009. Chemical structure in granitic magmas–a signal from the source?. Earth and Environmental Science Transactions of the Royal Society of Edinburgh 100, 159–172.

Collins, W. J., 1996. S-and I-type granites of the eastern Lachlan fold belt: products of three-component mixing. Transactions of the Royal Society of Edinburgh 88, 171–179.

Deshmukh, T., Prabhakar, N., Bhattacharya, A., Madhavan, K., 2017. Late Paleoproterozoic clockwise P–T history in the Mahakoshal Belt, Central Indian Tectonic Zone: Implications for Columbia supercontinent assembly. Precambrian Research 298, 56–78.

D'Souza, J., Prabhakar, N., Xu, Y., Sharma, K. K., Sheth, H., 2019. Mesoarchaean to Neoproterozoic (3.2–0.8 Ga) crustal growth and reworking in the Aravalli Craton, northwestern India: Insights from the Pur-Banera supracrustal belt. Precambrian Research 332. https://doi.org/10.1016/j. precamres.2019.105383

Goldstein, S. J., Jacobsen, S. B., 1988. Nd and Sr isotopic systematics of river water suspended material: implications for crustal evolution. Earth and Planetary Science Letters 87, 249–265.

Gopalan, K., Trivedi, J. R., Merh, S. S., Patel, P. P., Patel, S. G., 1979. Rb-Sr age of Godhra and related granites, Gujarat, India. Proceedings of the Indian Academy of Sciences A- 2, Earth and Planetary Science 88, 7–17.

Gorton, M. P., Schandl, E. S., 2000. From continents to island arcs: a geochemical index of tectonic setting for arc-related and within-plate felsic to intermediate volcanic rocks. The Canadian Mineralogist 38, 1065–1073.

Goscombe, B, Foster, D.A., Gray, D., Wade, B., Marsellos, A., Titus, J., 2017. Deformation correlations, stress field switches and evolution of an orogenic intersection: The Pan-African Kaoko-Damara orogenic junction, Namibia. Geoscience Frontiers 8, 1187–1232.

Goyal, N., Pant, P. C., Hansda, P. K., Pandey, B. K., 2001. Geochemistry and Rb-Sr age of the late Proterozoic Godhra granite of central Gujarat, India. Journal of the Geological Society of India 58, 391–398.

Gupta, P., Fareeduddin, R. M. S., Mukhopadhyay, K., 1995. Stratigraphy and structure of Delhi Supergroup of rocks in central part of Aravalli Range. Records of the Geological Survey of India 120, 12–26.

Hinchey, A. M., 2021., Lithogeochemical and Nd isotopic constraints on felsic magmatism in the Makkovik Orogen, Labrador, Canada: Implications for assembly of the supercontinent Nuna. Lithos 382, 105917. https://doi.org/10.1016/j.lithos.2020.105917

Horstwood, M. S., Košler, J., Gehrels, G., Jackson, S. E., McLean, N. M., Paton, C., Pearson, N. J., Sircombe, K., Sylvester, P., Vermeesch, P., Bowring, J. F., 2016. Community-derived standards for LA-ICP-MS U-(Th-) Pb geochronology–Uncertainty propagation, age interpretation and data reporting. Geostandards and

Geoanalytical Research 40, 311–332. https://doi.org/10.1111/j.1751-908X.2016.00379.x

Jackson, S. E., Pearson, N. J., Griffin, W. L., Belousova, E. A., 2004. The application of laser ablation-inductively coupled plasma-mass spectrometry to in situ U–Pb zircon geochronology. Chemical Geology 211, 47–69. https://doi.org/10.1016/j.chemgeo.2004.06.017

Jercinovic, M.J., Williams, M. L, 2005. Analytical perils (and progress) in electron microprobe trace element analysis applied to geochronology: back-ground acquisition, interferences, and beam irradiation effects. American Mineralogist 90, 526–546.

Joshi, A. U., Limaye, M. A., 2014. Evidence of syndeformational granitoid emplacement within Champaner Group, Gujarat. Journal of the Maharaja Sayajirao University of Baroda 49, 45–54.

Kaur, P., Zeh, A., Chaudhri, N., 2017. Paleoproterozoic continental arc magmatism, and Neoproterozoic metamorphism in the Aravalli-Delhi orogenic belt, NW India: New constraints from in-situ zircon U-Pb-Hf isotope systematic, monazite dating and whole rock geochemistry. Journal of Asian Earth Science 136, 68–88.

Kaur, P., Chaudhri, N., Eliyas, N., 2019. Origin of trondhjemite and albitite at the expense of A-type granite, Aravalli orogen, India: Evidence from new metasomatic replacement fronts. Geoscience Frontiers 10, 1891–1913. https://doi.org/10.1016/j.gsf.2018.09.019

Knöper, M,, Armstrong, R., Andreoli, M., Ashwal, L., 2000. The Steenkampskraal monazite vein: a subhorizontal stretching shear zone indicating extensional collapse of Namaqualand at 1033 Ma? Journal of African Earth Sciences 31, 38–38.

Kruhl, J. R., 1996. Prism- and basal-plane parallel subgrain boundaries in quartz: a microstructural geothermobarometer. Prism- and basal-plane parallel subgrain

boundaries in quartz: a microstructural geothermobarometer. Journal of Metamorphic Geology, 14, 581−589. https://doi.org/10.1046/j.1525-1314.1996.00413.x

Leelanandam, C., Burke, K., Ashwal, L.D., Webb, S.J., 2006. Proterozoic mountain building in Peninsular India: an analysis based primarily on alkaline rock distribution. Geological Magazine 143, 195–212.

Ludwig, K. R., 2012. Isoplot/Ex version 4.15, a geochronological toolkit for Microsoft Excel. Berkeley Geochronology Center Special Publication 4, 78.

Lugmair, G. W., Marti, K., 1978. Lunar initial $^{143}Nd/^{144}Nd$: differential evolution of the lunar crust and mantle. Earth and Planetary Science Letters 39, 349–357.

Macedo, J., Marshak, S., 1999. Controls on the geometry of fold -thrust belt salient. Geological Society of America Bulletin 111, 1808–1822. https://doi.org/10.1130/0016-7606(1999)111<1808:COTGOF>2.3.CO;2

Mamtani, M. A., Greiling, R. O., 2005. Granite emplacement and its relation with regional deformation in the Aravalli Mountain Belt (India)—inferences from magnetic fabric. Journal of Structural Geology 27, 2008–2029.

McDonough, W. F., Sun, S. S., 1995. The composition of the Earth. Chemical Geology 120, 223–253. https://doi.org/10.1016/0009-2541(94)00140-4

McKenzie, N. R., Hughes, N. C., Myrow, P. M., Banerjee, D. M., Deb, M., Planavsky, N. J., 2013. New age constraints for the Proterozoic Aravalli–Delhi successions of India and their implications. Precambrian Research 238, 120–128. https://doi.org/10.1016/j.precamres.2013.10.006

Montel, J. M., Foret, S., Veschambre, M., Provost, A., 1996. Electron microprobe dating of monazite. Chemical Geology 131, 37–53.

Mukherjee, S., Dey, A., Ibanez-Mejia, M., Sanyal, S. and Sengupta, P., 2018. Geochemistry, U-Pb geochronology and Lu-Hf isotope systematics of a suite of ferroan (A-type)

granitoids from the CGGC: Evidence for Mesoproterozoic crustal extension in the east Indian shield. Precambrian Research 305, 40–63.

Mukherjee, S., Adhikari, A., Vadlamani, R., 2019. Constraining paleoproterozoic (~ 1.7 Ga) collisional orogenesis between the Eastern Dharwar and Bastar cratons: New Sm–Nd garnet isochron and Th–U-total Pb monazite chemical ages from the Bhopalpatnam orogen, central India. Lithos 350, 105247.

Naha, K., Mukhopadhyay, D. K., Mohanty, R., Mitra, S. K., Biswal, T. K., 1984. Significance of contrast in the early stages of the structural history of the Delhi and the pre-Delhi rock group in the Proterozoic of Rajasthan, western India. Tectonophysics 105, 193–206.

Patchett, P. J., 1989. Radiogenic Isotope Geochemistry of Rare Earth Elements, In: Lipin, B. R., McKay, G. A. (Eds) Geochemistry and mineralogy of rare earth elements, Reviews in Mineralogy 21, Mineralogical Society of America, Washington, D.C., USA-20006, 25–41.

Patiño Douce, A. E., Beard, J. S., 1996. Effects of P, f(O_2) and Mg/Fe ratio on dehydration melting of model metagreywackes. Journal of Petrology 37, 999–1024.

Paton, C., Hellstrom, J., Paul, B., Woodhead, J., Hergt, J., 2011. Iolite: Freeware for the visualisation and processing of mass spectrometric data. Journal of Analytical Atomic Spectrometry 26, 2508–2518. https://doi.org/10.1039/C1JA10172B

Prabhakar, N., 2013. Resolving poly-metamorphic Paleoarchean ages by chemical dating of monazites using multi-spectrometer U, Th and Pb analyses and sub-counting methodology. Chemical Geology 347, 257–270.

Rollinson, H., Pease, V., 2021. Using geochemical data: To understand geological processes. 2nd edition. Cambridge University Press. Cambridge. https://doi.org/10.1017/9781108777834

Roy, A. B., Kröner, A., 1996. Single zircon evaporation ages constraining the growth of the Archaean Aravalli craton, northwestern Indian shield. Geological Magazine 133, 333–342. https://doi.org/ 10.1017/S0016756800009067

Rudnick, R. L., Gao, S., 2003. Composition of the continental crust, In: Holland, H. D., Turekian, K. K., (Eds) The crust, Treatise on Geochemistry 3, 1–64.

Sahni, A., Tandon, S.K., Jolly, A., Bajpai, S., Sood, A., Srinivasan, S., 1994. Upper Cretaceous dinosaur eggs and nesting sites from the Deccan-volcano sedimentary province of peninsular India. In: Carpenter,K., Hirsch, K.F., Horner, J.R. (Eds.), Dinosaur Eggs and Babies, Cambridge University Press, New York, 204–226.

Sequeira, N., Bhattacharya, A., 2021. Early Neoproterozoic accretion at the northern margin of the Chottanagpur Gneiss Complex, Eastern India. Tectonics 40, e2020TC006613, https://doi.org/10.1029/2020TC006613.

Sequeira, N., Mahato, S., Rahl, J., Sarkar, S., Bhattacharya, A., 2020. The anatomy and origin of a syn-convergent Grenvillian age metamorphic core complex, Chottanagpur Gneiss Complex, Eastern India. Lithosphere 2020, doi:https://doi.org/10.2113/2020/8833404

Sequeira, N., Bhattacharya, A., Bell, E., 2021. The ~1.4 Ga A-type granitoids in the "Chottanagpur crustal block" (India), and its relocation from Columbia to Rodinia? Geoscience Frontiers (in press). https://doi.org/10.1016/j.gsf.2020.12.017

Sharma R. S., 2009. Cratons of the Indian Shield. In: Cratons and Fold Belts of India. Lecture Notes in Earth Sciences. Springer, Berlin, Heidelberg, 127 https://doi.org/10.1007/978-3-642-01459-8_2

Shivkumar, K., Maithani, P. B., Parthasarathy, R. N., Dwivedy, K. K., 1993. Proterozoic rift in lower Champaners and its bearing in uranium mineralisation in Panchmahals district, Gujarat. In: Annual convention of the Geological Society of India (Abstracts), Department of Geology, Maharaja Sayajirao University of Baroda, Vadodara.

Sivaraman, T. V., Odom, A. L., 1982. Zircon geochronology of Berach granite of Chittorgarh, Rajasthan. Journal of the Geological Society of India 23, 575–577.

Spear, F. S., Pyle, J. M., Cherniak, D., 2009. Limitations of chemical dating of monazite. Chemical Geology 266, 218–230.

Srimal, N., Das, S., 1998. On the tectonic affinity of the Champaner Group of rocks, Eastern Gujarat. Abstract Volume, International Seminar on the Precambrian Crustal Evolution of Central and Eastern India. UNESCO-lUGS-IGCP-368. Bhubaneswar, 226–227.

Stacey, J.T., Kramers, J.D., 1975. Approximation of terrestrial lead isotope evolution by a two-stage model. Earth and Planetary Science Letters 26, 207–221.

Steiger, R. H., Jäger, E., 1977. Subcommission on geochronology: convention on the use of decay constants in geo-and cosmochronology. Earth and Planetary Science Letters 36, 359–362.

Sylvester, P. J., 1998. Post-collisional strongly peraluminous granites. Lithos 45, 29–44.

Tanaka, T., Togashi, S., Kamioka, H., Amakawa, H., Kagami, H., Hamamoto, T., Yuhara, M., Orihashi, Y., Yoneda, S., Shimizu, H., Kunimaru, T., 2000. JNdi-1: a neodymium isotopic reference in consistency with LaJolla neodymium. Chemical Geology 168, 279–281. https://doi.org/10.1016/S0009-2541(00)00198-4

Thirlwall, M. F., Anczkiewicz, R., 2004. Multidynamic isotope ratio analysis using MC–ICP–MS and the causes of secular drift in Hf, Nd and Pb isotope ratios. International Journal of Mass Spectrometry 235, 59–81. https://doi.org/10.1016/j.ijms.2004.04.002

Vermeesch, P., 2018. IsoplotR: a free and open toolbox for geochronology. Geoscience Frontiers 9, 1479–1493. 10.1016/j.gsf.2018.04.001.

Velandia, F., García-Delgado, H., Zuluaga, C. A., López, J. A., Bermúdez, M. A., Audemard F.A., 2020. Present-day structural frame of the Santander Massif and Pamplona

Wedge: The interaction of the Northern Andes. Journal of Structural Geology 137, 104087. https://doi.org/10.1016/j.jsg.2020.104087

Vielzeuf, D., Schmidt, M. W., 2001. Melting relations in hydrous systems revisited: application to metapelites, metagreywackes and metabasalts. Contributions to Mineralogy and Petrology 141, 251–267. https://doi.org/10.1007/s004100100237

Wang, W., Cawood, P. A., Pandit, M. K., Zhou, M. F., Chen, W. T., 2017. Zircon U–Pb age and Hf isotope evidence for an Eoarchaean crustal remnant and episodic crustal reworking in response to supercontinent cycles in NW India. Journal of the Geological Society of India 174, 759–772. https://doi.org/10.1144/jgs2016-080

Watson, E. B., Harrison, T. M., 1983. Zircon saturation revisited: temperature and composition effects in a variety of crustal magma types. Earth and Planetary Science Letters 64, 295–304. https://doi.org/10.1016/0012-821X(83)90211-X

Weil, A. B., Sussman, A., 2004, Classification of curved orogens based on the timing relationships between structural development and vertical-axis rotation. In: Sussman, A.J., Weil, A.B. (Eds.), Orogenic Curvature: Integrating Paleomagnetic and Structural Analyses. Geological Society of America Special Paper 383, 1–17.

Whalen, J. B., Currie, K. L., Chappell, B. W., 1987. A-type granites: geochemical characteristics, discrimination and petrogenesis. Contributions to Mineralogy and Petrology 95, 407–419.

Wiedenbeck, M. A. P. C., Alle, P., Corfu, F., Griffin, W. L., Meier, M., Oberli, F. V., Quadt, A. V., Roddick, J. C., Spiegel, W., 1995. Three natural zircon standards for U-Th-Pb, Lu-Hf, trace element and REE analyses. Geostandards Newsletter 19, 1–23. https://doi.org/10.1111/j.1751-908X.1995.tb00147.x

Wiedenbeck, M., Goswami, J. N., Roy, A. B., 1996. Stabilization of the Aravalli Craton of northwestern India at 2.5 Ga: an ion microprobe zircon study. Chemical Geology 129, 325–340. https://doi.org/10.1017/S0016756800009067

Winter, J. D., 2001. Chemical Petrology II: Trace elements and isotopes, In: Lynch, P., Griffith, A. (Eds). An introduction to igneous and metamorphic petrology. Prentice Hall Inc., Upper Saddle, New Jersey, 155–180.

Yang, Z., Tang, J., Santosh, M., Zhao, X., Lang, X., Wang, Y., Ding, S., Ran, F., 2021. Microcontinent subduction and S-type volcanism prior to India–Asia collision. Scientific Reports 11, 1–13. https://doi.org/10.1038/s41598-021-94492-y

Zhu, Z., Campbell, I. H., Allen, C. M., Burnham, A. D., 2020. S-type granites: Their origin and distribution through time as determined from detrital zircons. Earth and Planetary Science Letters 536, 116140. https://doi.org/10.1016/j.epsl.2020.116140

Declaration of interests

☒The authors declare that they have no known competing financial interests or personal relationships that could have appeared to influence the work reported in this paper.

☐The authors declare the following financial interests/personal relationships which may be considered as potential competing interests:

Highlights

1. Godhra-Chhota Udepur (GC) is the western end of the Central Indian Tectonic Zone [83]
2. At GC, NNE-SSW shortening is contemporaneous with 0.95–0.93 Ga felsic emplacements [85]
3. In north GC, 2.5 Ga granite reworked at 0.95 Ga with no Paleoproterozoic overprint [85]
4. In south GC, no Archean inheritance noted in 1.6 Ga gneisses reworked at 0.95 Ga [83]
5. ~0.95 Ga accretion welded mutually exclusive Archean and Paleoproterozoic terrains [85]

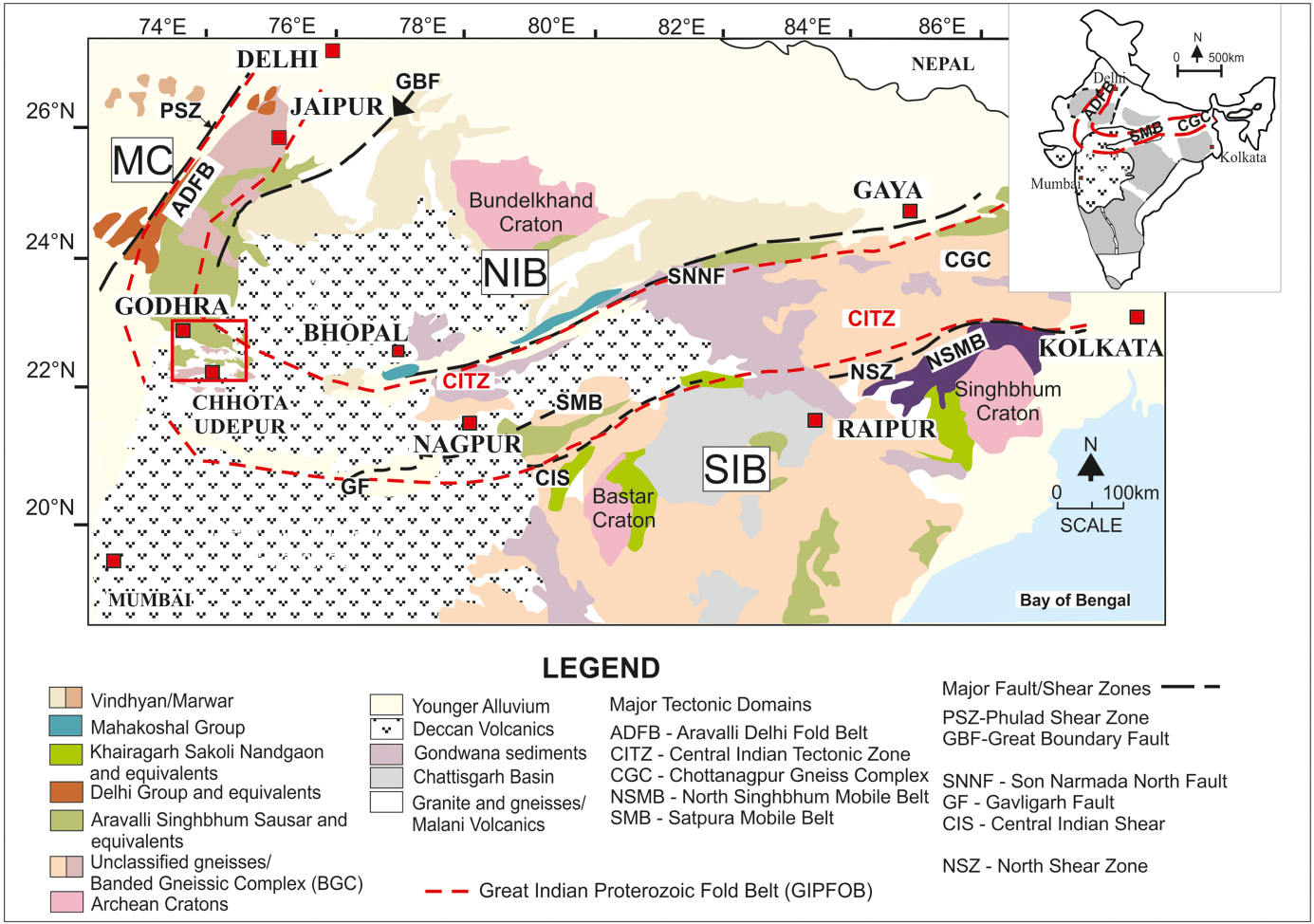
74°E
76°E
78°E
80°E
82°E
84°E
86°E
26°N
24°N
22°N
20°N
DELHI
GBF
PSZ
JAIPUR
MC
ADFB
NEPAL
Bundelkhand Craton
NIB
GAYA
CGC
SNNF
GODHRA
BHOPAL
CITZ
KOLKATA
NSZ
NSMB
Singhbhum Craton
CHHOTA UDEPUR
SMB
NAGPUR
RAIPUR
CIS
SIB
GF
Bastar Craton
N
0 100km
SCALE
MUMBAI
Bay of Bengal
N
0 500km
Delhi
Mumbai
Kolkata
ADFB
SMB
CGC
LEGEND
Vindhyan/Marwar
Mahakoshal Group
Khairagarh Sakoli Nandgaon and equivalents
Delhi Group and equivalents
Aravalli Singhbhum Sausar and equivalents
Unclassified gneisses/ Banded Gneissic Complex (BGC)
Archean Cratons
Younger Alluvium
Deccan Volcanics
Gondwana sediments
Chattisgarh Basin
Granite and gneisses/ Malani Volcanics
Major Tectonic Domains
ADFB - Aravalli Delhi Fold Belt
CITZ - Central Indian Tectonic Zone
CGC - Chottanagpur Gneiss Complex
NSMB - North Singhbhum Mobile Belt
SMB - Satpura Mobile Belt
Major Fault/Shear Zones
PSZ-Phulad Shear Zone
GBF-Great Boundary Fault
SNNF - Son Narmada North Fault
GF - Gavligarh Fault
CIS - Central Indian Shear
NSZ - North Shear Zone
Great Indian Proterozoic Fold Belt (GIPFOB)

Figure 1

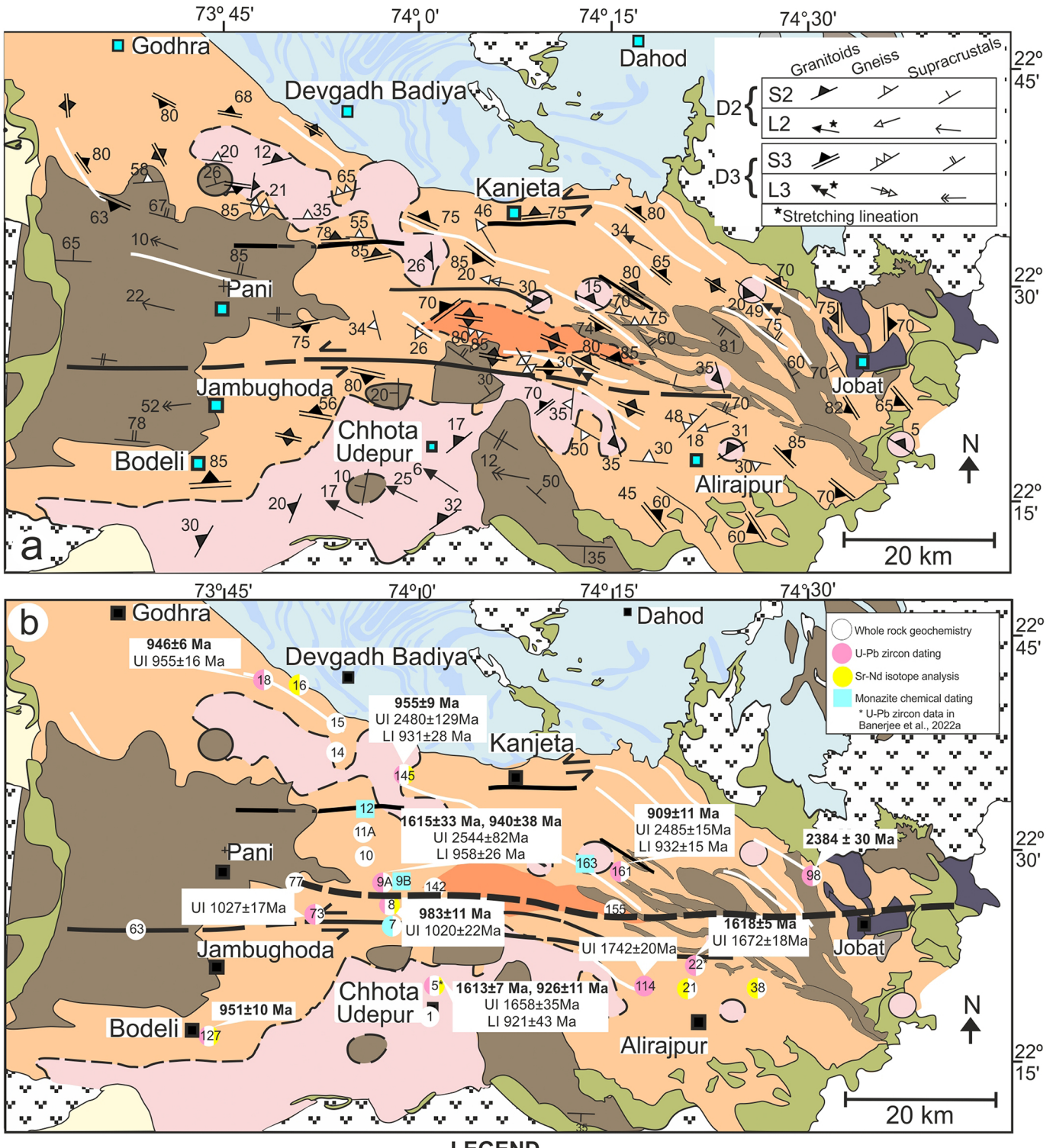
73° 45'
74° 0'
74° 15'
74° 30'
22° 45'
22° 30'
22° 15'
Godhra
Dahod
Devgadh Badiya
Kanjeta
Pani
Jambughoda
Chhota Udepur
Bodeli
Alirajpur
Jobat
Granitoids
Gneiss
Supracrustals
D2
S2
L2
D3
S3
L3
*Stretching lineation
N
20 km
a
b
Whole rock geochemistry
U-Pb zircon dating
Sr-Nd isotope analysis
Monazite chemical dating
* U-Pb zircon data in Banerjee et al., 2022a
946±6 Ma
UI 955±16 Ma
955±9 Ma
UI 2480±129Ma
LI 931±28 Ma
1615±33 Ma, 940±38 Ma
UI 2544±82Ma
LI 958±26 Ma
909±11 Ma
UI 2485±15Ma
LI 932±15 Ma
2384 ± 30 Ma
UI 1027±17Ma
983±11 Ma
UI 1020±22Ma
1618±5 Ma
UI 1672±18Ma
UI 1742±20Ma
1613±7 Ma, 926±11 Ma
UI 1658±35Ma
LI 921±43 Ma
951±10 Ma
LEGEND
Younger Alluvium
Bagh/Lameta (Infra/Intertrappean) Beds
Deccan Volcanics
Mafic/Ultramafic rocks of Aravalli Supergroup
Supracrustal rocks (Lunavada Group)
Supracrustal rocks (Champaner Group)
Sanada granite pluton
Gneisses and granitoids (shallow carapace)
Gneisses and granitoids

Figure 2

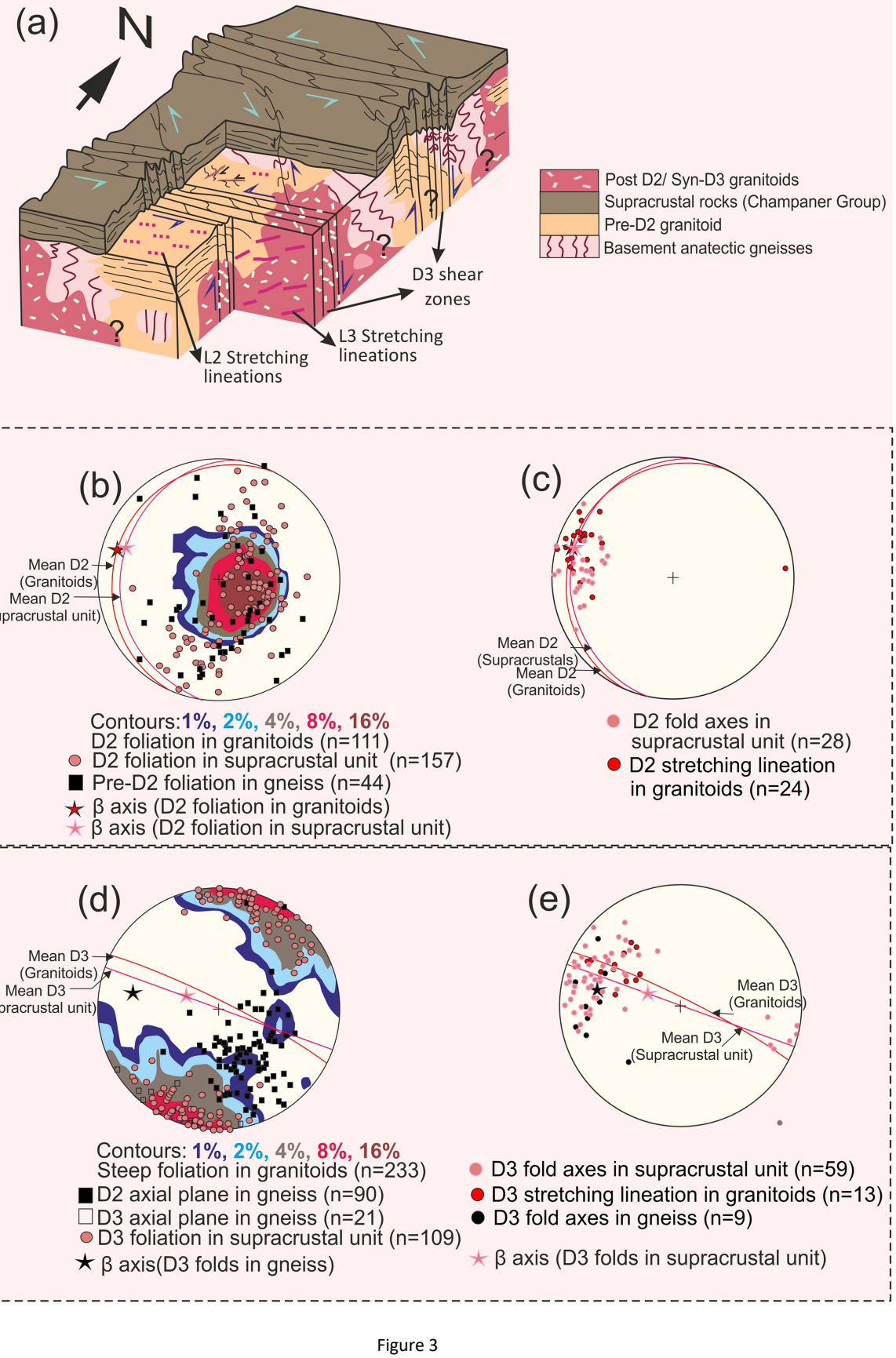
(a)
N
Post D2/ Syn-D3 granitoids
Supracrustal rocks (Champaner Group)
Pre-D2 granitoid
Basement anatectic gneisses
D3 shear zones
L3 Stretching lineations
L2 Stretching lineations
D2 deformation
(b)
Mean D2 (Granitoids)
Mean D2 (Supracrustal unit)
Contours:1%, 2%, 4%, 8%, 16%
D2 foliation in granitoids (n=111)
D2 foliation in supracrustal unit (n=157)
Pre-D2 foliation in gneiss (n=44)
β axis (D2 foliation in granitoids)
β axis (D2 foliation in supracrustal unit)
(c)
Mean D2 (Supracrustals)
Mean D2 (Granitoids)
D2 fold axes in supracrustal unit (n=28)
D2 stretching lineation in granitoids (n=24)
D3 deformation
(d)
Mean D3 (Granitoids)
Mean D3 (Supracrustal unit)
Contours: 1%, 2%, 4%, 8%, 16%
Steep foliation in granitoids (n=233)
D2 axial plane in gneiss (n=90)
D3 axial plane in gneiss (n=21)
D3 foliation in supracrustal unit (n=109)
β axis(D3 folds in gneiss)
(e)
Mean D3 (Granitoids)
Mean D3 (Supracrustal unit)
D3 fold axes in supracrustal unit (n=59)
D3 stretching lineation in granitoids (n=13)
D3 fold axes in gneiss (n=9)
β axis (D3 folds in supracrustal unit)

Figure 3

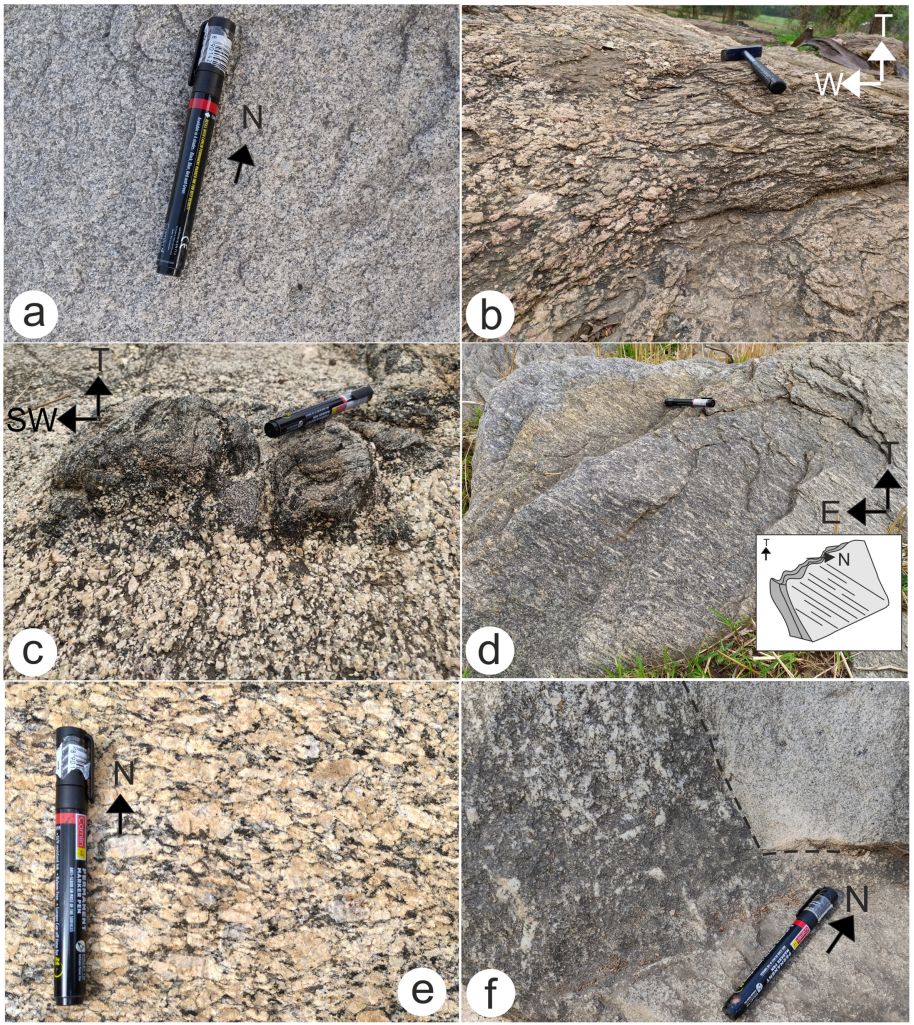

Figure 4

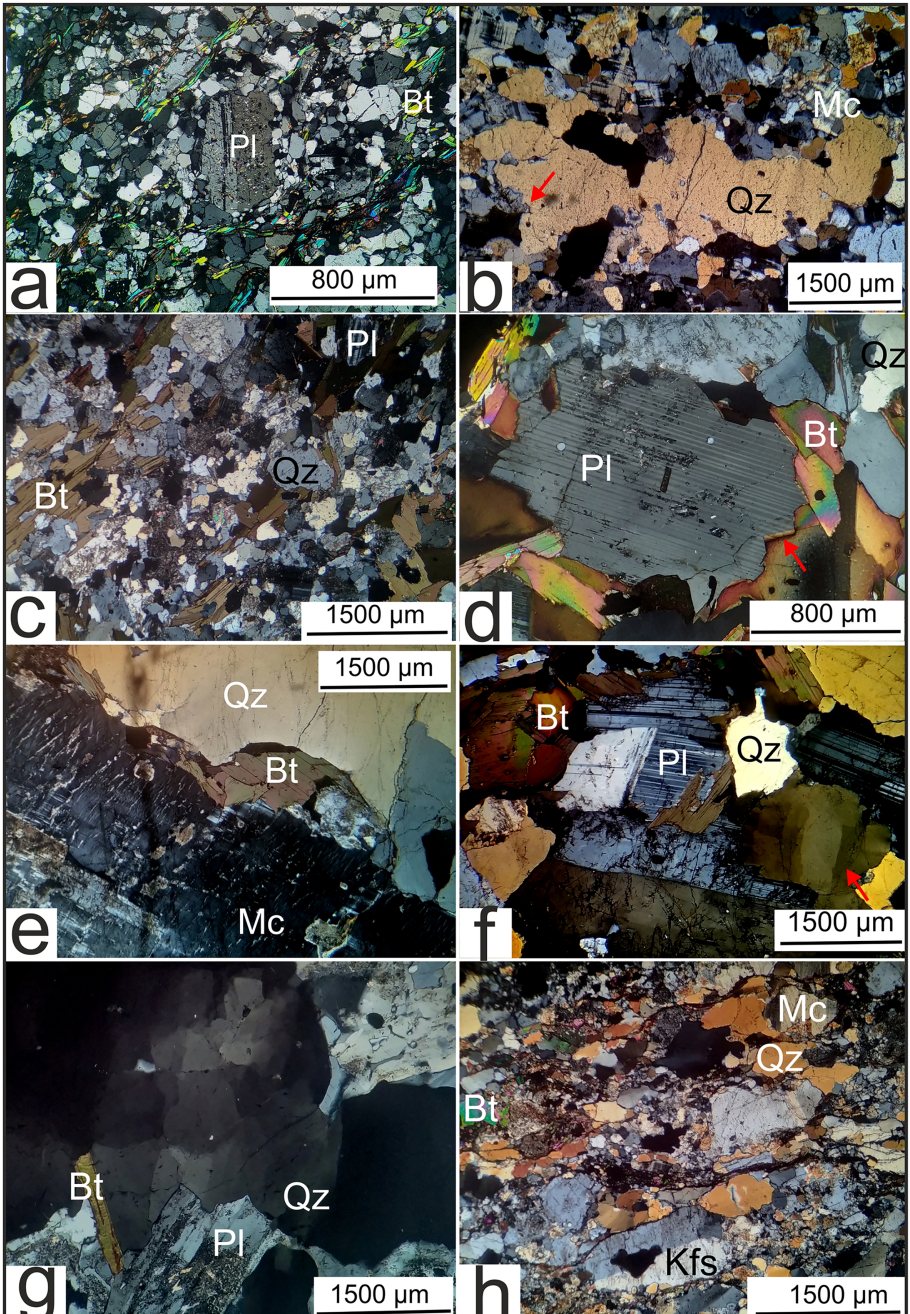
a
Bt
Pl
800 µm
b
Mc
Qz
1500 µm
c
Pl
Qz
Bt
1500 µm
d
Qz
Bt
Pl
800 µm
e
1500 µm
Qz
Bt
Mc
f
Bt
Pl
Qz
1500 µm
g
Bt
Qz
Pl
1500 µm
h
Mc
Qz
Bt
Kfs
1500 µm

Figure 5

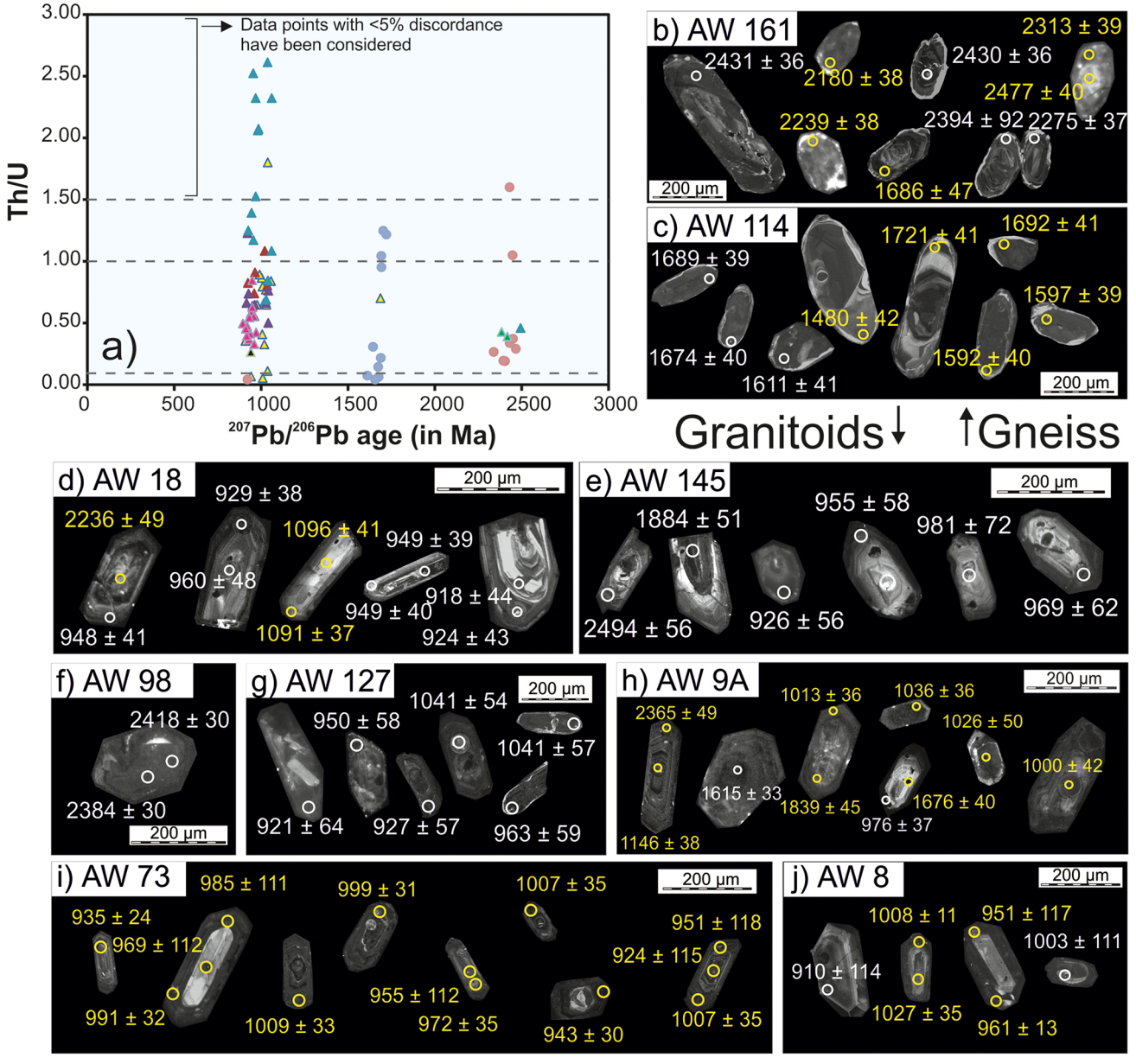
a)
Th/U
3.00
2.50
2.00
1.50
1.00
0.50
0.00
0
500
1000
1500
2000
2500
3000
Data points with <5% discordance have been considered
207Pb/206Pb age (in Ma)
b) AW 161
2313 ± 39
2431 ± 36
2430 ± 36
2180 ± 38
2477 ± 40
2239 ± 38
2394 ± 92
2275 ± 37
1686 ± 47
200 µm
c) AW 114
1721 ± 41
1692 ± 41
1689 ± 39
1597 ± 39
1480 ± 42
1674 ± 40
1592 ± 40
1611 ± 41
200 µm
Granitoids↓
↑Gneiss
d) AW 18
200 µm
929 ± 38
2236 ± 49
1096 ± 41
949 ± 39
960 ± 48
918 ± 44
949 ± 40
948 ± 41
1091 ± 37
924 ± 43
e) AW 145
200 µm
1884 ± 51
955 ± 58
981 ± 72
2494 ± 56
926 ± 56
969 ± 62
f) AW 98
2418 ± 30
2384 ± 30
200 µm
g) AW 127
200 µm
1041 ± 54
950 ± 58
1041 ± 57
921 ± 64
927 ± 57
963 ± 59
h) AW 9A
200 µm
1013 ± 36
1036 ± 36
2365 ± 49
1026 ± 50
1000 ± 42
1615 ± 33
1839 ± 45
1676 ± 40
976 ± 37
1146 ± 38
i) AW 73
200 µm
985 ± 111
999 ± 31
1007 ± 35
935 ± 24
951 ± 118
969 ± 112
924 ± 115
955 ± 112
991 ± 32
1009 ± 33
972 ± 35
943 ± 30
1007 ± 35
j) AW 8
200 µm
1008 ± 11
951 ± 117
1003 ± 111
910 ± 114
1027 ± 35
961 ± 13

Figure 6

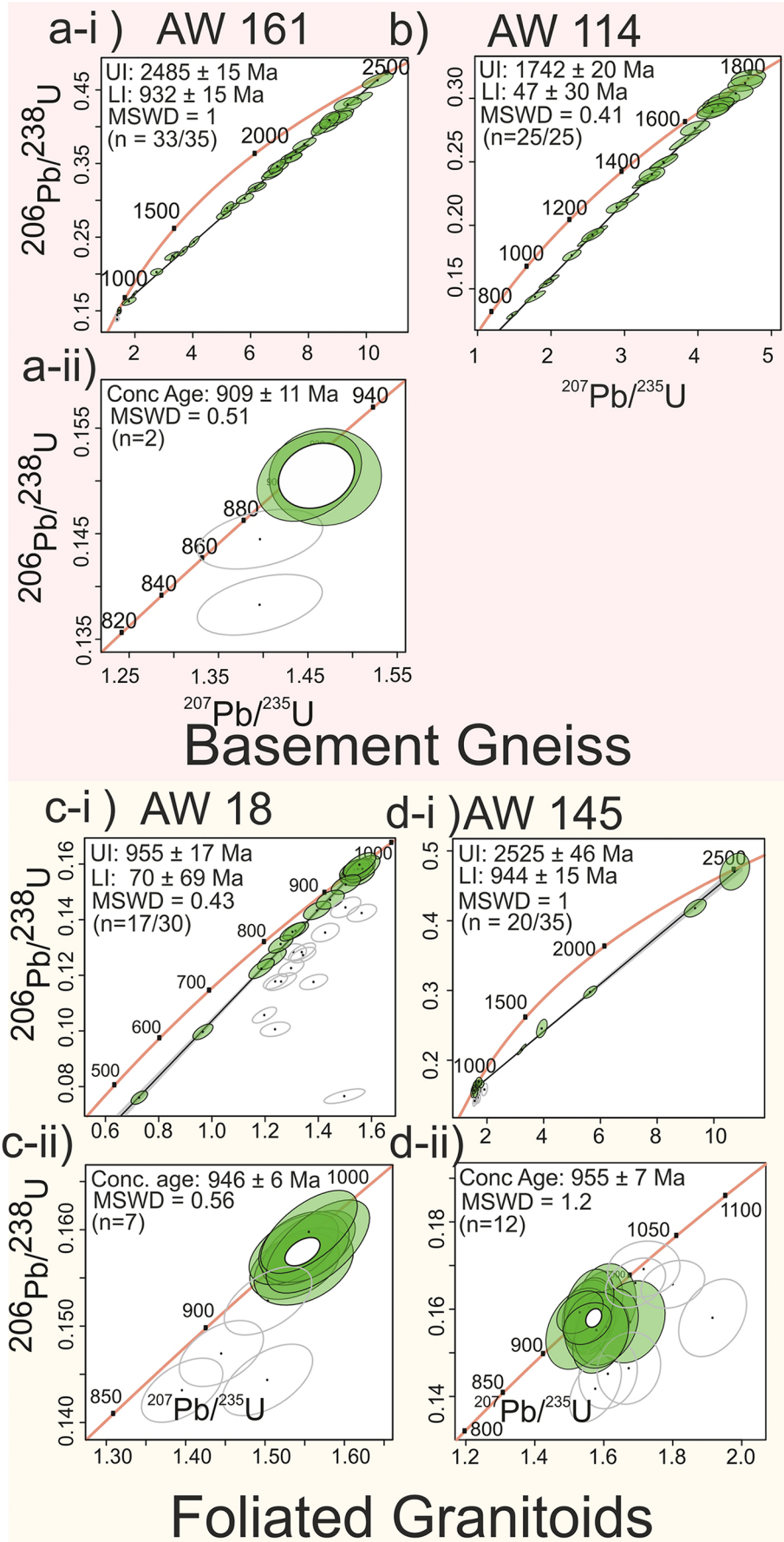
a-i) AW 161
UI: 2485 ± 15 Ma
LI: 932 ± 15 Ma
MSWD = 1
(n = 33/35)
2500
2000
1500
1000
$^{206}Pb/^{238}U$
a-ii)
Conc Age: 909 ± 11 Ma
MSWD = 0.51
(n=2)
940
880
860
840
820
$^{207}Pb/^{235}U$
b) AW 114
UI: 1742 ± 20 Ma
LI: 47 ± 30 Ma
MSWD = 0.41
(n=25/25)
1800
1600
1400
1200
1000
800
$^{207}Pb/^{235}U$
Basement Gneiss
c-i) AW 18
UI: 955 ± 17 Ma
LI: 70 ± 69 Ma
MSWD = 0.43
(n=17/30)
1000
900
800
700
600
500
$^{206}Pb/^{238}U$
c-ii)
Conc. age: 946 ± 6 Ma
MSWD = 0.56
(n=7)
1000
900
850
$^{207}Pb/^{235}U$
d-i)AW 145
UI: 2525 ± 46 Ma
LI: 944 ± 15 Ma
MSWD = 1
(n = 20/35)
2500
2000
1500
1000
d-ii)
Conc Age: 955 ± 7 Ma
MSWD = 1.2
(n=12)
1100
1050
900
850
800
$^{207}Pb/^{235}U$
Foliated Granitoids

Figure 7A

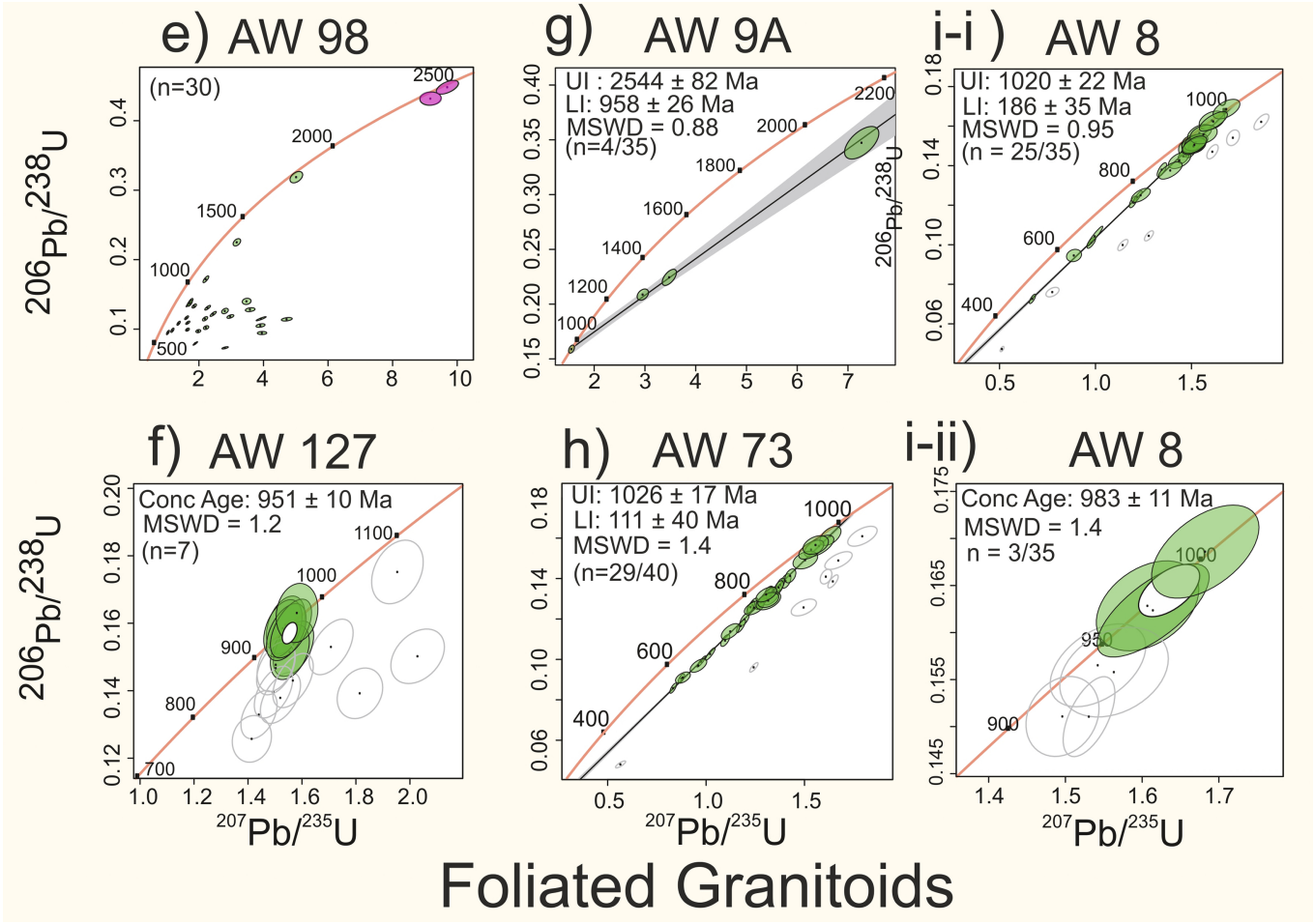
e) AW 98
(n=30)
2500
2000
1500
1000
500
$^{206}Pb/^{238}U$
g) AW 9A
UI : 2544 ± 82 Ma
LI: 958 ± 26 Ma
MSWD = 0.88
(n=4/35)
2200
2000
1800
1600
1400
1200
1000
$^{206}Pb/^{238}U$
i-i) AW 8
UI: 1020 ± 22 Ma
LI: 186 ± 35 Ma
MSWD = 0.95
(n = 25/35)
1000
800
600
400
f) AW 127
Conc Age: 951 ± 10 Ma
MSWD = 1.2
(n=7)
1100
1000
900
800
700
$^{206}Pb/^{238}U$
$^{207}Pb/^{235}U$
h) AW 73
UI: 1026 ± 17 Ma
LI: 111 ± 40 Ma
MSWD = 1.4
(n=29/40)
1000
800
600
400
$^{207}Pb/^{235}U$
i-ii) AW 8
Conc Age: 983 ± 11 Ma
MSWD = 1.4
n = 3/35
1000
950
900
$^{207}Pb/^{235}U$
Foliated Granitoids

Figure 7B

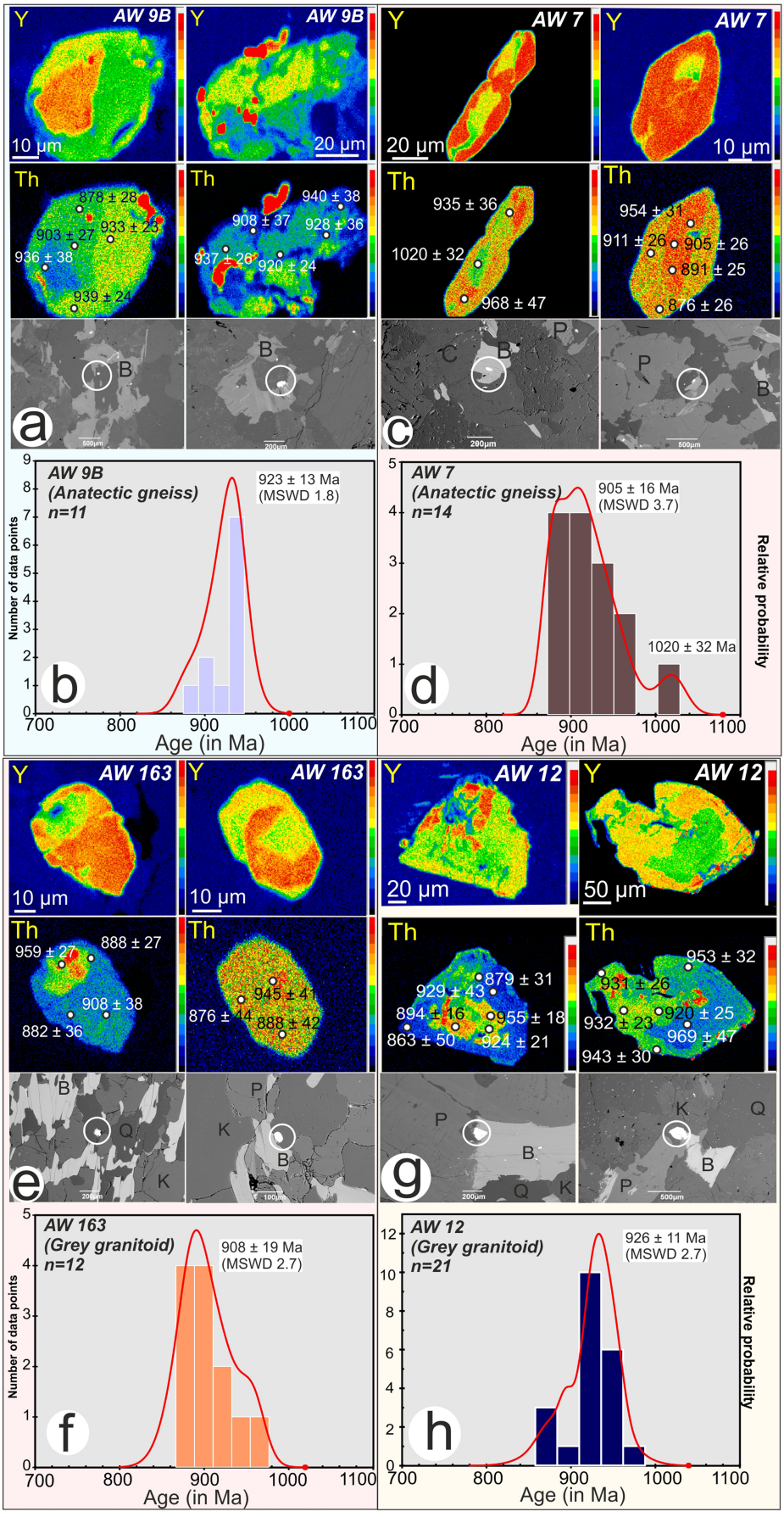
Y
AW 9B
10 µm
Y
AW 9B
20 µm
Y
AW 7
20 µm
Y
AW 7
10 µm
Th
878 ± 28
903 ± 27
933 ± 23
936 ± 38
939 ± 24
Th
940 ± 38
908 ± 37
928 ± 36
937 ± 26
920 ± 24
Th
935 ± 36
1020 ± 32
968 ± 47
Th
954 ± 31
911 ± 26
905 ± 26
891 ± 25
876 ± 26
B
B
C
B
P
P
B
a
c
AW 9B
(Anatectic gneiss)
n=11
923 ± 13 Ma
(MSWD 1.8)
Number of data points
b
Age (in Ma)
AW 7
(Anatectic gneiss)
n=14
905 ± 16 Ma
(MSWD 3.7)
1020 ± 32 Ma
Relative probability
d
Age (in Ma)
Y
AW 163
10 µm
Y
AW 163
10 µm
Y
AW 12
20 µm
Y
AW 12
50 µm
Th
959 ± 27
888 ± 27
908 ± 38
882 ± 36
Th
945 ± 41
876 ± 44
888 ± 42
Th
879 ± 31
929 ± 43
894 ± 16
55 ± 18
863 ± 50
924 ± 21
Th
953 ± 32
931 ± 26
920 ± 25
932 ± 23
969 ± 47
943 ± 30
B
Q
K
P
K
B
P
B
Q
K
K
Q
B
P
e
g
AW 163
(Grey granitoid)
n=12
908 ± 19 Ma
(MSWD 2.7)
Number of data points
f
Age (in Ma)
AW 12
(Grey granitoid)
n=21
926 ± 11 Ma
(MSWD 2.7)
Relative probability
h
Age (in Ma)

Figure 8

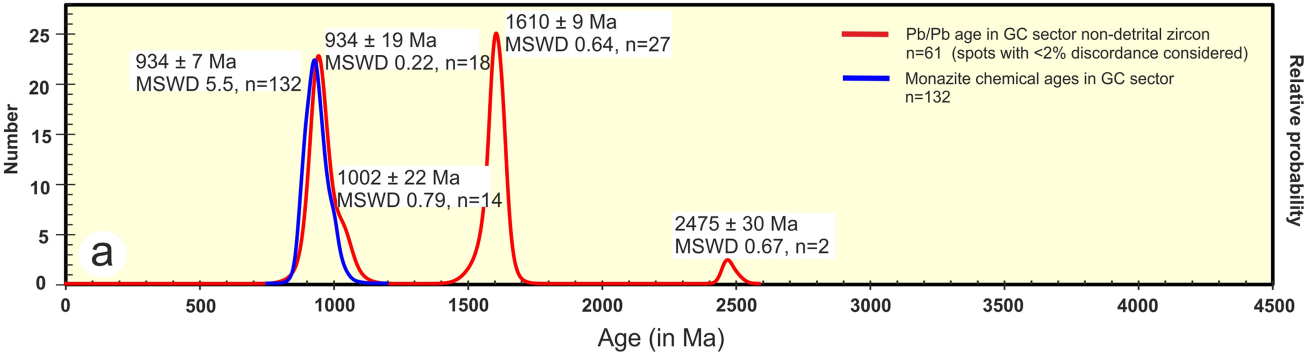
934 ± 7 Ma
MSWD 5.5, n=132
934 ± 19 Ma
MSWD 0.22, n=18
1610 ± 9 Ma
MSWD 0.64, n=27
1002 ± 22 Ma
MSWD 0.79, n=14
2475 ± 30 Ma
MSWD 0.67, n=2
Pb/Pb age in GC sector non-detrital zircon
n=61 (spots with <2% discordance considered)
Monazite chemical ages in GC sector
n=132
a
Number
Relative probability
Age (in Ma)
0
5
10
15
20
25
0
500
1000
1500
2000
2500
3000
3500
4000
4500

Figure 9

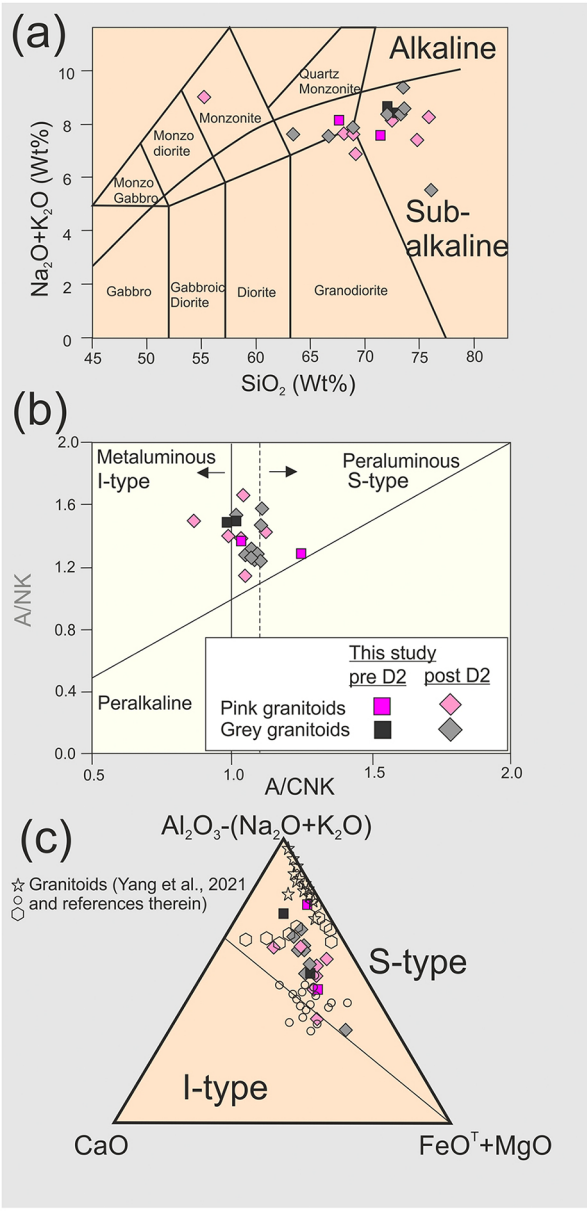
(a)
Alkaline
Sub-alkaline
Quartz Monzonite
Monzonite
Monzo diorite
Monzo Gabbro
Gabbro
Gabbroic Diorite
Diorite
Granodiorite
Na2O+K2O (Wt%)
SiO2 (Wt%)
(b)
Metaluminous I-type
Peraluminous S-type
Peralkaline
A/NK
A/CNK
This study
pre D2
post D2
Pink granitoids
Grey granitoids
(c)
Al2O3-(Na2O+K2O)
Granitoids (Yang et al., 2021 and references therein)
S-type
I-type
CaO
FeOT+MgO
(d)
Gneiss samples (This study)
Garnetiferous gneiss AW142 (This study)
ΣREE
Eu/Eu*
(e)
Nb/Ta
Nb/Ta=5
Ta (ppm)
(f)
Nb/Ta
Barren granites
Rare metal related granites
Ta-Cs-Li-Nb-Be-Sn-W
Sn-W-(U) related granites
Zr/Hf
(g)
Th/Ta
A. Felsic and intermediate rocks:Oceanic arcs
B. Felsic and intermediate rocks:
Active continental margins
C. Felsic and intermediate rocks:
Within plate volcanics
D. MORB and within plate basalts
A
B
C
D
Yb (ppm)
CGC granitoids; Sequeira et al., 2021
CGC granitoids; Mukherjee et al., 2018
SMB granitoids; Chattopadhyay et al., 2015
SMB granitoids; Chattopadhyay et al., 2017

Figure 10

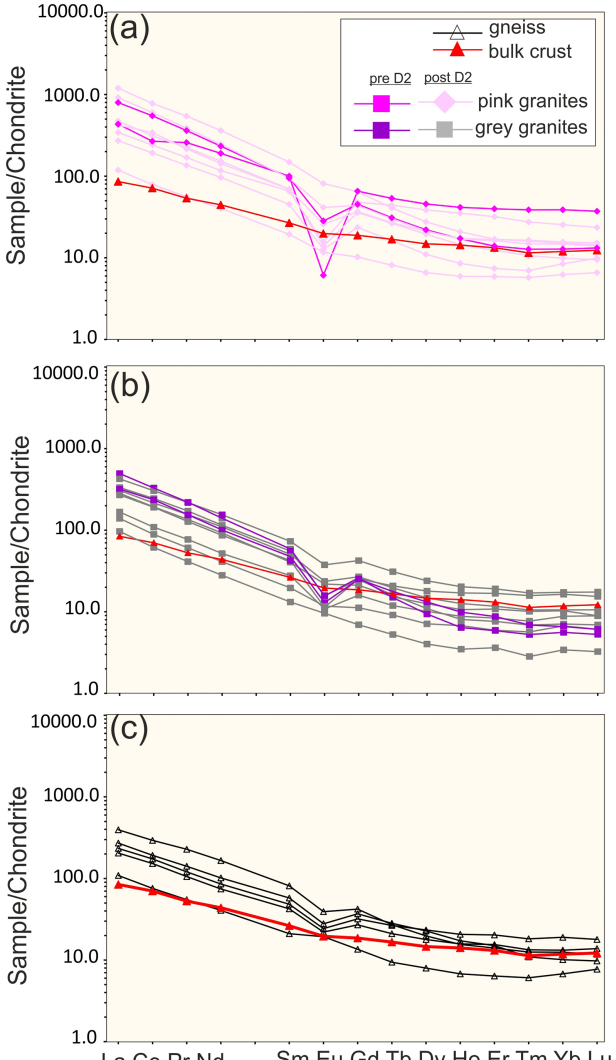
(a)
(b)
(c)
gneiss
bulk crust
pre D2
post D2
pink granites
grey granites
Sample/Chondrite
10000.0
1000.0
100.0
10.0
1.0
La Ce Pr Nd Sm Eu Gd Tb Dy Ho Er Tm Yb Lu

Figure 11

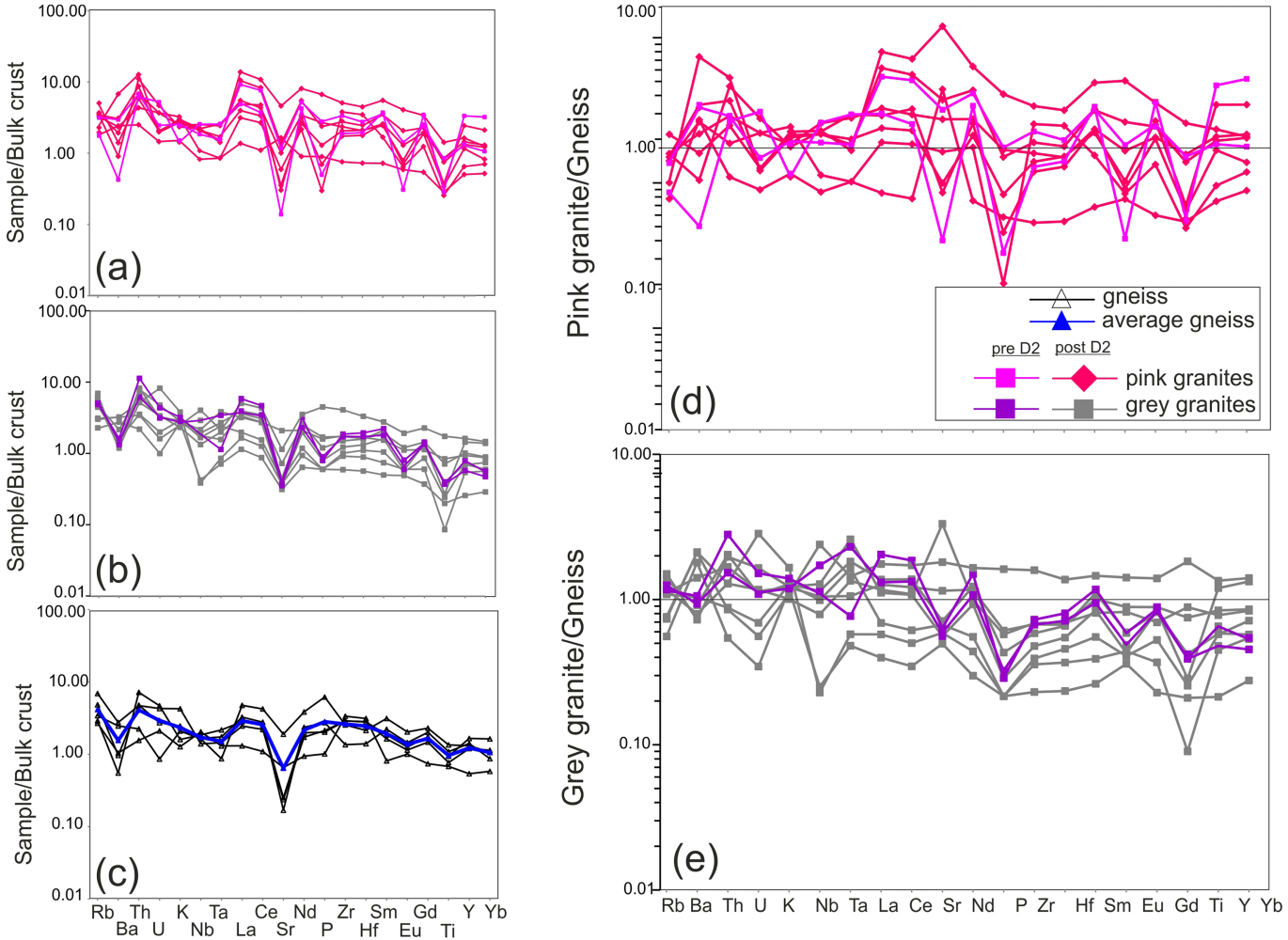
Sample/Bulk crust
100.00
10.00
1.00
0.10
0.01
(a)
(b)
(c)
Rb Th K Ta Ce Nd Zr Sm Gd Y Yb
Ba U Nb La Sr P Hf Eu Ti
Pink granite/Gneiss
Grey granite/Gneiss
(d)
(e)
gneiss
average gneiss
pre D2
post D2
pink granites
grey granites
Rb Ba Th U K Nb Ta La Ce Sr Nd P Zr Hf Sm Eu Gd Ti Y Yb

Figure 12

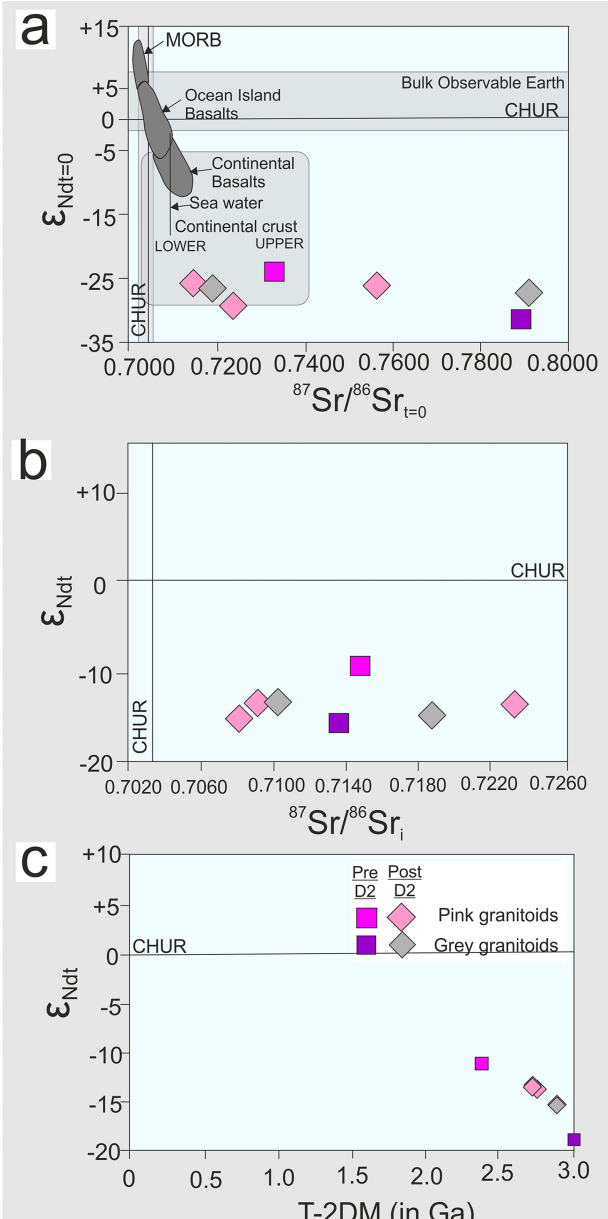
a
+15
+5
0
-5
-15
-25
-35
εNdt=0
MORB
Ocean Island Basalts
Bulk Observable Earth
CHUR
Continental Basalts
Sea water
Continental crust
LOWER
UPPER
CHUR
0.7000 0.7200 0.7400 0.7600 0.7800 0.8000
87Sr/86Sr t=0
b
+10
0
-10
-20
εNdt
CHUR
CHUR
0.7020 0.7060 0.7100 0.7140 0.7180 0.7220 0.7260
87Sr/86Sr i
c
+10
+5
0
-5
-10
-15
-20
εNdt
CHUR
Pre D2
Post D2
Pink granitoids
Grey granitoids
0 0.5 1.0 1.5 2.0 2.5 3.0
T-2DM (in Ga)

Figure 13

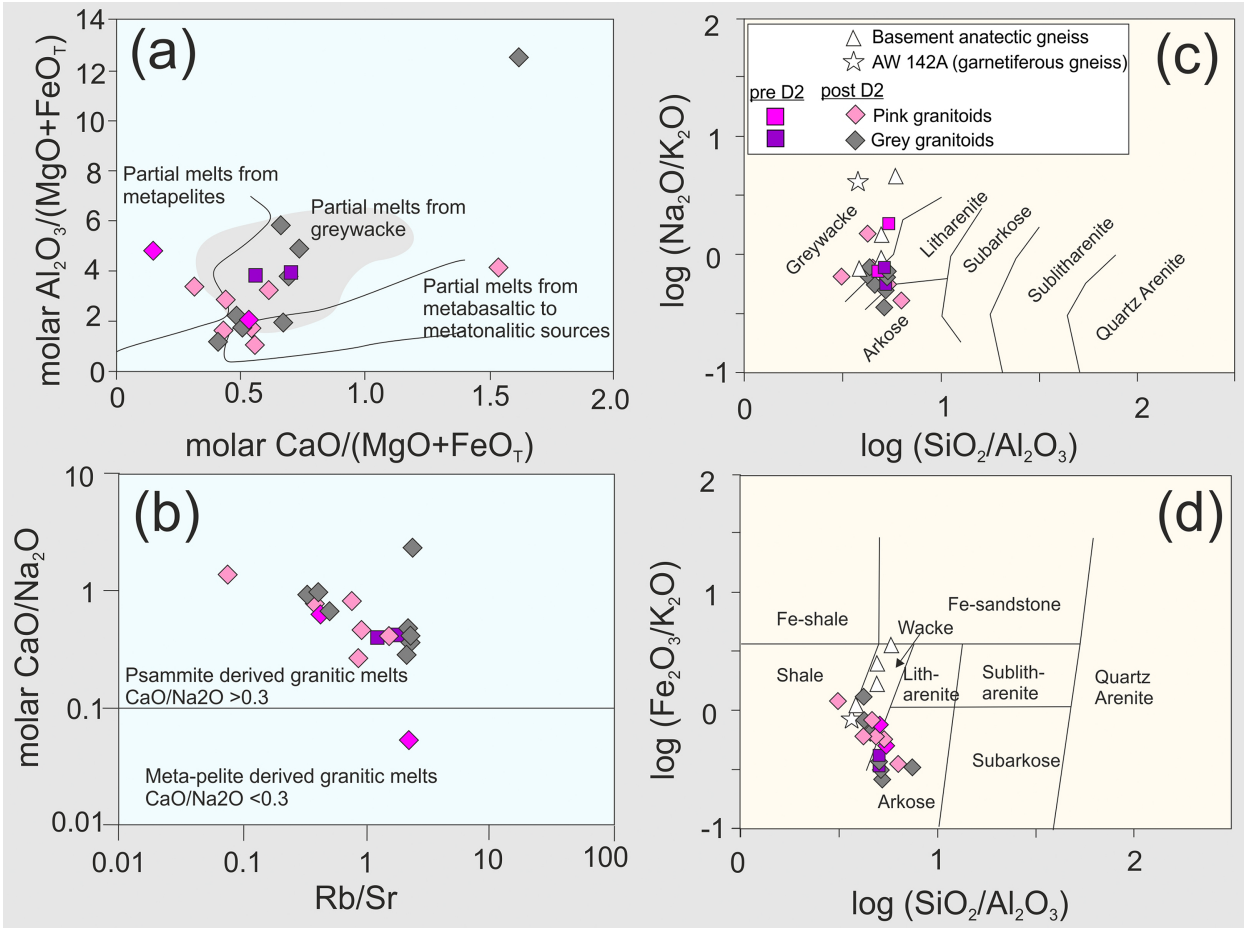
(a)
molar $Al_2O_3/(MgO+FeO_T)$
molar $CaO/(MgO+FeO_T)$
Partial melts from metapelites
Partial melts from greywacke
Partial melts from metabasaltic to metatonalitic sources
(b)
molar CaO/Na_2O
Rb/Sr
Psammite derived granitic melts
CaO/Na2O >0.3
Meta-pelite derived granitic melts
CaO/Na2O <0.3
(c)
Basement anatectic gneiss
AW 142A (garnetiferous gneiss)
pre D2
post D2
Pink granitoids
Grey granitoids
log (Na_2O/K_2O)
log (SiO_2/Al_2O_3)
Greywacke
Litharenite
Subarkose
Sublitharenite
Quartz Arenite
Arkose
(d)
log (Fe_2O_3/K_2O)
log (SiO_2/Al_2O_3)
Fe-shale
Wacke
Fe-sandstone
Shale
Lith-arenite
Sublith-arenite
Quartz Arenite
Subarkose
Arkose

Figure 14